

CFD simulations of an isolated cycling spoked wheel: Impact of the ground and wheel/ground contact modeling

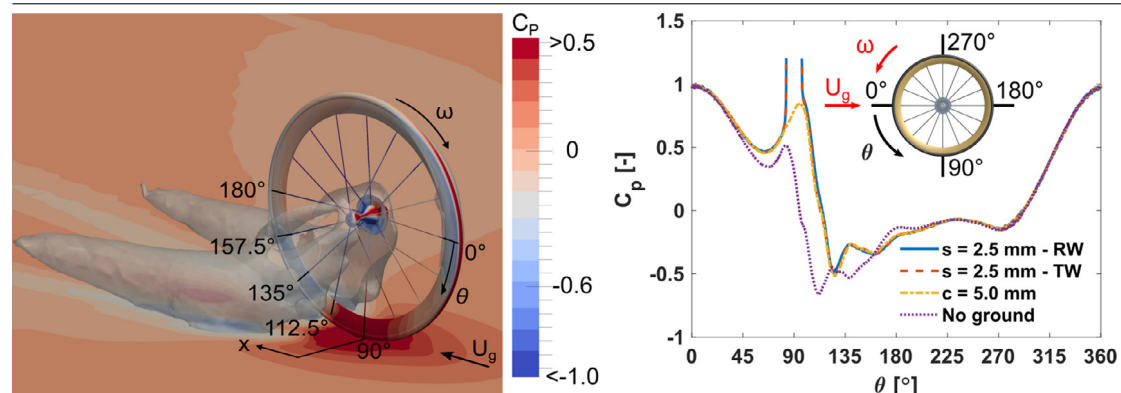
Fabio Malizia*, Bert Blocken

Department of Civil Engineering, KU Leuven, Leuven, Belgium

Department of the Built Environment, Eindhoven University of Technology, Eindhoven, The Netherlands



GRAPHICAL ABSTRACT



ARTICLE INFO

Article history:

Received 29 October 2019

Received in revised form 6 February 2020

Accepted 11 February 2020

Available online 24 February 2020

Keywords:

Cycling spoked wheel

CFD simulations

Wheel/ground contact modeling

Cycling aerodynamics

ABSTRACT

Spoked wheels are the most frequently used wheel type in road cycling competitions and their aerodynamic optimization is crucial for cyclist performance. The aerodynamic performance of wheels is generally analyzed by wind tunnel tests or CFD simulations for isolated wheels. There is a large number of options to model the wheel/ground contact in CFD simulations, including different clearances between tire and ground and different heights of solid contact patches (step). However, it is unclear to what extent these modeling options influence the CFD results. The present paper systematically analyzes the impact of these options on the computed forces and moments of an isolated cycling spoked wheel and elucidates the flow behavior around this wheel for zero yaw conditions. The wheel drag coefficient for the cases where the ground is included in the simulations using a clearance or a step is 1.0% and about 1.8% lower compared to the case without ground, respectively, whereas the rotational moment is about 2.0% lower for all the wheel/ground contact modeling approaches compared to the case without ground. The gap clearance (≤ 20 mm) and step height (≤ 10 mm) should be kept minimal to avoid a significant influence on the forces and moments. In addition, the presence of the ground influences the flow behavior in the lower section of the wheel including the pressure distribution on the exterior of the wheel. This study is intended to help researchers and manufacturers to perform accurate CFD simulations of cycling spoked wheels and to optimize their aerodynamics.

© 2020 The Authors. Published by Elsevier Masson SAS. This is an open access article under the CC BY-NC-ND license (<http://creativecommons.org/licenses/by-nc-nd/4.0/>).

1. Introduction

Aerodynamic drag is the major resistive force for a cyclist, up to 90% of the total resistance when riding on flat terrain at racing speeds of about 40 km/h [1,2]. The aerodynamic drag is mainly

* Corresponding author at: Department of Civil Engineering, KU Leuven, Leuven, Belgium.

E-mail address: fabio.malizia@kuleuven.be (F. Malizia).

caused by the cyclist body, which generally accounts for 60% to 82% of the total drag depending on his/her position on the bicycle [2–4], whereas the remaining drag is caused by the bicycle. Despite the lower contribution by the bicycle, its aerodynamic optimization is crucial to improve the overall performance of elite cyclists considering that races are sometimes won based on time differences of seconds or fractions of a second, or on distance differences of only a few centimeter. For example, Greg Lemond gained 58 s to Laurent Fignon in the 24.5 km individual time-trial of the Tour de France 1989 between Versailles and Paris, winning that Tour de France by only 8 s. Primož Roglič gained 26 s to Adam Yates in the 10.05 km individual time-trial of the Tirreno-Adriatico 2019 in San Benedetto del Tronto, winning that Tirreno-Adriatico by only 0.31 s. Kristina Vogel won the gold medal in the track cycling sprint competition of the Rio 2016 Olympic games with a margin of only 0.016 s and 0.004 s against Becky James in race 1 and race 2, respectively; where each race had a 200 m length with a flying start.

To understand how aerodynamic drag reduction influences the total time of a race, several cycling mathematical models were developed [5–7]. For instance, Martin et al. [7] stated that only a 2% reduction of the combined cyclist–bicycle drag area would already lead to time savings of 0.030 s, 0.120 s and 0.314 s for three different cyclists on a 250 m, 500 m and 1000 m track race, respectively. As a result, the bicycle aerodynamics can significantly impact the final performance of elite cyclists and the outcome of cycling competitions.

The bicycle consists of several elements, among which the frame, wheels and handlebar are considered most relevant for aerodynamic drag reduction. According to Greenwell et al. [8], the two wheels can account for 10% of the total cyclist–bicycle drag. Therefore a lot of effort to improve the aerodynamics of cycling wheels has been spent in the past years and several manufacturers nowadays provide a large variety of wheels: in the Tour de France 2019, for example, the 22 cycling teams were equipped with wheels from 12 different wheel manufacturers [9], each of them listing several wheel types in their catalogue. This situation with many different wheels creates the need for well accepted methodologies to investigate wheel aerodynamic performance, so that different wheels can be correctly compared in terms of their aerodynamics.

The standard practice in the assessment of the aerodynamic performance of cycling wheels, either by wind tunnel (WT) tests or computational fluid dynamics (CFD) simulations, is to focus on isolated wheels. Here, the term isolated refers to the absence of the frame but with the inclusion of a slender support structure in WT tests, and with potential presence of a nearby flat surface, roller or rolling belt representing the ground. While it is clear that the final goal is the drag reduction of the whole system of the bicycle – including all components – and rider, testing wheels together with the rest of the bicycle unavoidably renders the results on wheel performance dependent on the bicycle and the rider (e.g. in [10,11]), which complicates a clear comparison. Therefore, the vast majority of previous WT [8,12–20] and CFD studies [21–26] of cycling wheel aerodynamics were performed for isolated wheels (see Tables 1 and 2). Note that even studies on car wheel aerodynamics often focus on isolated wheels (e.g. [27–29]), although in car aerodynamics the interaction between the wheels and car body is more pronounced than in cycling on regular bicycles (i.e. not recumbent bicycles or hand-cycles).

But even with the focus generally on isolated wheels, Crane and Morton [20] pointed out that the testing protocols might significantly vary between different manufacturers and researchers. This might explain the very large drag coefficient discrepancies reported in Godo et al. [23] for different WT tests of the same wheel: at zero degree yaw angle, the drag coefficient varied

between 0.017 and 0.051 for the Zipp 404, between 0.021 and 0.050 for the Zipp 808 and between 0.016 and 0.041 for the Zipp Sub9 disc wheel. Note that several WT results reported in [23] were provided by cycling manufacturers: it is unclear whether these data were subjected to scientific reporting and peer review and therefore these data have to be considered as unsubstantiated and hence should be treated with caution. In some cases wheels were tested with different type of supports, which can even further inhibit a proper comparison of wheel performance. As an example, Greenwell et al. [8] and Tew and Sayers [17] performed WT tests of the Campagnolo Shamal spoked wheel and the Specialized trispoke wheel. The measured drag by Tew and Sayers [17] was 37% and 16% lower than the measured drag by Greenwell et al. [8], for the spoked and tri-spoke wheel, respectively. These discrepancies were likely caused by the different test conditions: different WTs were employed; open test section in [17] versus closed test section in [8], probably different tires were used, 20 mm width in [17] versus not provided by [8], different wheel types were applied, a front wheel in [17] and a rear wheel including gears in [8] and finally, different wheel supports were used; a single vertical strut in [17] versus the rear part of a cut bicycle frame in [8]. Table 1 reports these and other WT studies of cycling wheels. A more detailed literature review on the aerodynamic testing of cycling wheels is provided in [26].

The above-mentioned lack of uniform testing methodology in WT experimentation is also observed in CFD simulations of cycling wheels, as shown by the large variety of computational settings between different studies in Table 2. Therefore, Malizia et al. [26] investigated the impact of three computational parameters on the computed forces and moments: the spatial discretization, the wheel rotation modeling and the turbulence modeling. This study considered an isolated wheel without the presence of the ground, similar to the WT experiments of Tew and Sayers [17] that were used for validation purposes. It was shown that each of these three parameters had a strong influence on the resulting forces and moments, therefore some guidelines were proposed which should guide and uniform future CFD simulations of cycling spoked wheels.

However, this previous study [26] did not consider the effect of the presence of the ground and the contact between wheel and ground on the resulting forces and moments. In most CFD simulations in Table 2, the ground was present and the wheel/ground contact was modeled either with a gap or a step, although no information was provided about the size of this gap or step. The lack of such information renders it difficult to compare the results from the different studies in terms of the impact of the wheel/ground contact modeling. Because the presence of the ground and the wheel/ground contact might substantially modify the forces and moments acting on the wheels, the ground has to be included in the CFD simulations when the aerodynamic comparison of different wheels is the main focus. In car aerodynamics, the wheel/ground contact was already found to have a large impact on the measured aerodynamic forces acting on the wheels and on the flow behavior, both in WT experiments [30–32] and CFD simulations [28,33,34]. Ideally, the tire is tangential to the ground, however, a real tire is deformed when in contact with the ground, thus creating a contact patch or footprint. The size of this footprint is influenced by many variables, such as the load on the wheel and the tire stiffness [28]. Therefore, rotating the wheel while obtaining the correct wheel deformation adds significant complexity to WT experiments. The wheel/ground contact modeling also represents a challenge in CFD simulations: in addition to the correct reproduction of the wheel shape near the ground, issues arise due to the presence of highly skewed cells near the intersection line between the ground and the wheel. In previous studies on car wheel aerodynamics, this problem was overcome

by modeling the contact patch using a small solid step [27,28], as shown in Fig. 1a. Diasinos et al. [28] compared the impact of the step height “*s*” to the forces – drag and lift – and to the wake of a racing car wheel: increasing the step height, the wake squeezed laterally and increased in height. Diasinos et al. [28] argued that this behavior was caused by the variation in the contact patch aspect ratio for different step heights: increasing the step height, the contact patch increases more in the streamwise direction than in the spanwise direction. Moreover, a 20% drag coefficient reduction was computed for the wheel when the step height increased from 0.00280 to 0.00850, with \varnothing ($=0.416$ m) being the wheel diameter in this study [28], as shown in Fig. 1b.

However, car wheels and cycling wheels differ in many aspects. First, the wheel size is significantly different: a car wheel has a width of around 200 mm and a diameter between about 400 mm and 640 mm [28,31,35,36], whereas a bicycle wheel has a tire width of around 20 mm and a diameter of around 700 mm. Moreover, the bicycle spokes are thin and numerous while the car spokes have larger dimensions and are few in number. Lastly, the wheel rotational speed is significantly different: bicycle wheel tests are performed up to speeds of 50 km/h while car wheels can be tested or simulated also for speeds equal to or above 100 km/h [36,37]. Consequently, the maximum wheel rotational speed is about 40 rad/s for bicycle wheels [23], while car wheels are also tested at rotational speeds of 134 rad/s [37] and beyond. In addition, for regular bicycles (i.e. not recumbent or hand-cycles), the largest fraction of the volume of the combined cyclist-bicycle system is situated above the wheels, very different from the situation with cars and car wheels. Therefore, a different impact of the wheel/ground contact to the measured forces between the car and bicycle wheels might be expected. Greenwell et al. [8] stated that the “ground effects are likely to be small” for bicycle wheels. However, to the best of our knowledge, the impact of the ground on the forces and moments of cycling wheels has never been reported, neither based on WT experiments nor based on CFD simulations. Note that for hand-cycling, part of the para-cycling family, the situation is different and a larger impact of the ground on the forces acting on the hand-cycle is expected because the body of bicycle (frame) and cyclist are much closer to the wheels and to the ground in the vertical direction [38–40].

This paper intends to investigate the impact of the ground contact modeling of an isolated cycling spoked wheel on the aerodynamic forces and moments acting on this wheel. This is performed considering two different approaches for the wheel/ground contact modeling. In the first, the wheel is displaced from the ground, the tire is considered to be undeformed by the ground and a gap is present between the bottom of the wheel/tire and the ground. This approach has been used frequently in previous CFD studies of cycling aerodynamics [41–43]. In the second approach, the wheel deformation due to the contact is represented by a solid volume or “step” that replaces the contact patch (Fig. 1b). In the latter approach, two different boundary conditions are applied to the step: rotating wall or translating wall.

Section 2 describes the WT experiments of Greenwell et al. [8] that are used for CFD validation. Section 3 presents the CFD settings, including a description of the selected wheel for this study (Campagnolo Shamal rear wheel). The results are presented in Section 4 including the grid sensitivity study (Section 4.1), the CFD validation (Section 4.2) and the impact of wheel/ground contact modeling (Section 4.3). Finally, discussion and conclusions are provided in Sections 5 and 6.

2. Wind tunnel measurements

Greenwell et al. [8] tested seven rear wheels, including three spoked wheels (conventional 36-spoke wheel, Campagnolo Shamal 16-spoke and HED CX 24-spoke wheel), two trispoke wheels (Specialized and FIR trispoke) and two disc wheels (HED and ZIPP).

The measurements were performed in a closed test section WT with uniform approach flow-conditions and a turbulence intensity of 0.5%. The test section had an octagonal cross-sectional shape of 2.13×1.52 m² (7×5 ft²) width and height, with fillets of 0.31 m (~ 1 ft) dimension. The test section length was 2.52 m (~ 8.25 ft). The wheel was suspended from the top of the WT test section (Fig. 2a) and placed at 1.1 m distance from the beginning of the test section [44]. The height of the gap between the wheel and the surface of the wind tunnel ceiling was not specified. Rear wheels were employed because the rear section of a cut bicycle frame was used as support in the WT (Fig. 2a). Moreover, the wheel was rotated by a DC motor connected to the wheel by a bicycle chain. The forces and moments were measured for the support with and without the wheel, so the support contribution to the total force could be removed. However, other corrections to the results were not described and the measurement accuracy was not reported. As an indication about the likely measurement accuracy in the experiments of Greenwell et al. [8], the present authors report that the measurement accuracy for the drag force on an isolated wheel was 0.10 N and 0.02 N in Kyle [13] and Tew and Sayers [17], respectively. Note that the latter two studies reported measurements performed in about the same time period (late 1980s–1990s). The validation in the present paper is performed against a study from 1995. In the past twenty-five years, measurement techniques and their accuracy have undoubtedly improved. However, up to the present day and to the best of our knowledge, no similarly extensive and well documented set of experimental data on wheel aerodynamics has been published in the peer-reviewed literature.

In the present study, the Campagnolo Shamal rear wheel was selected. This wheel is described in more detail in Section 3.1. Greenwell et al. [8] tested the Campagnolo Shamal wheel at three so-called “ground speeds” U_g equal to 4.47, 8.94 and 13.41 m/s (10, 20 and 30 mph). The WT velocity was fixed to U_r , computed as the vector sum between U_g and the wind velocity U_w , where the latter was also set equal to 4.47, 8.94 or 13.41 m/s (10, 20 and 30 mph) and at a wind angle θ between 0° and 90° from the U_g velocity vector. The resulting wheel yaw angle varied between 0° and 75°, as resultant of the vector sum between U_g and U_w . The results were provided in terms of the drag coefficient, C_D (Fig. 2b), the side force coefficient and the yawing moment coefficient. In addition to the drag coefficient, the rotational moment coefficient C_M is also considered in the present study due to its importance in the aerodynamic wheel performance [12,19]. These coefficients are defined as:

$$C_D = \frac{D}{0.5\rho AU_r^2} \quad (1)$$

$$C_M = \frac{M}{0.5\rho ArU_r^2} \quad (2)$$

where D and M are the drag force and the rotational moment (Fig. 3), ρ is the air density, A the reference area, r the wheel radius (including tire), and U_r the relative velocity. The reference area is the full side area of a wheel, thus equal to $A = \pi r^2 = 0.385$ m². This reference area is preferred over the frontal area $\varnothing \cdot t$, with \varnothing the wheel diameter (including tire) and t the tire width, because the frontal area can provide misleading results when wheels are tested with different tire widths, since a wider tire might provide the wheel with a lower drag coefficient but a higher drag [8].

Table 1

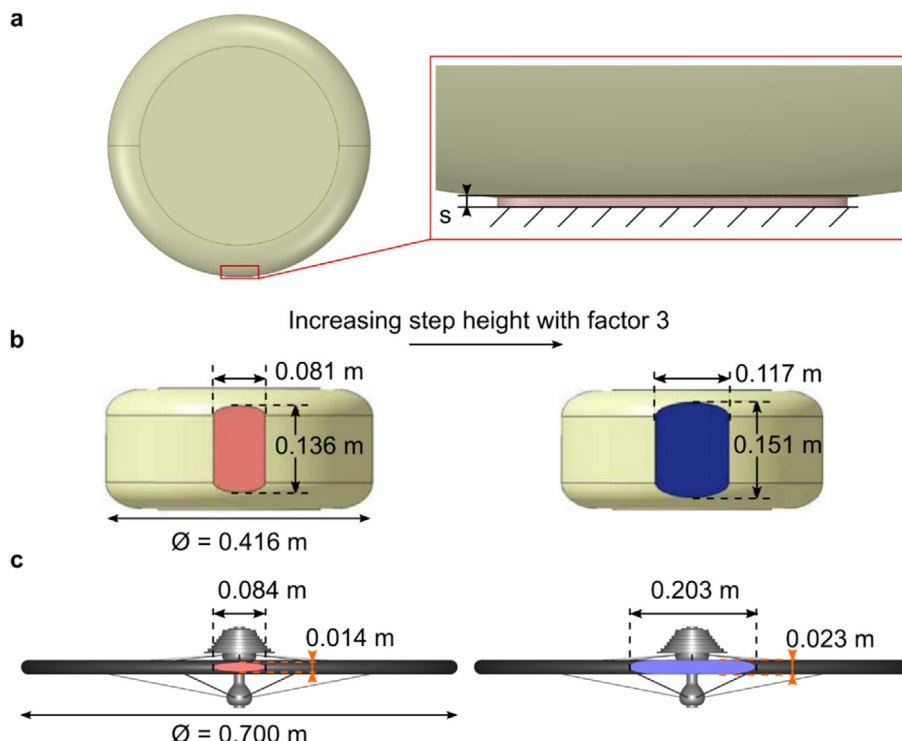
Wind tunnel tests of cycling-wheel aerodynamics.

Reference	Test-section [m^2]	Speed [km/h]	Wheel tested ^b	Isolated	Wheel/ground contact modeling	Reported results ^e	Rotational moment
[12–15]	0.61×0.91	24–73	Sp; a-Sp; disc	Yes	Non specified gap ^d	D	Yes
[16]	1.20×0.91	20–42	p-Sp	Yes	Non specified gap ^d	C_D, C_S, C_Y ^f	No
[18]	0.87×0.58^a	30–72	c-Sp	Yes	No ground	C_D ^f	No
[8]	1.52×2.13	16–48	Sp; a-Sp; disc	Yes ^c	Non specified gap ^d	C_D, C_S, C_Y ^g	No
[17]	0.87×0.58^a	30–55	Sp; a-Sp; disc	Yes	No ground	C_D, C_S ^g	No
[19]	0.90×1.20	30–50	Sp; a-Sp; disc	Yes	Gap < 4 mm	D, S, P	Yes
[10]	2.60×4.00^a	50	Sp; a-Sp; disc	Bicycle and rider	In contact	$C_D A, C_S A, C_Y A, C_R A$	No
[20]	1.00×1.00^a	32–59	Sp	Yes	In contact	$C_D A, C_S A$	No

^aOpen test section. The dimensions refer to the wind tunnel jet.^bSp = spoked; a-Sp = aero-spoked wheels (tri-spoke, four-spoke and five-spoke wheels); p-Sp = spoked wheels with splitter plates; c-Sp = spoked wheels with cladding; disc = disc or lenticular wheels.^cThe wheels in [8] were mounted on the rear section of a cut bicycle frame.^dThe presence of a gap was deducted from the figures or from the text in the original source. However, no further details were provided by the authors.^eD = drag; S = side force; C_D = drag coefficient; C_S = side force coefficient; C_Y = yawing moment coefficient; P = power; $C_D A$ = drag area; $C_S A$ = side force area; $C_Y A$ = yawing moment area; $C_R A$ = rolling moment area.^fDrag coefficient computed using frontal area, $2tr$, where t is the tire width and r the wheel radius including the tire.^gDrag coefficient computed using lateral area, πr^2 , where r is the wheel radius including the tire.**Table 2**

CFD simulations of cycling-wheel aerodynamics.

Reference	Wheel ^a	Domain ($W \times H \times L$) [m^3]	Grid size	Isolated	Wheel/ground contact modeling	Comparison with WT tests
[21]	Sp; a-Sp; disc	$1.4 \times 1.2 \times 5.0$	1 M – 6 M	Yes	Non specified gap ^d	No
[22,23]	Sp; a-Sp; disc	$1.4 \times 1.1 \times 2.8^b$	3.8 M – 16 M	Yes	Non specified step height	Yes
[11]	Sp; a-Sp; disc	Semi-ellipsoid ^c	6 M – 10 M	Front cut-bicycle frame	Non specified step height	Yes
[24]	Sp	$4.2 \times 4.2 \times 14.0$	250 k – 522 k	Yes	Non specified gap ^d	Yes ^e
[25]	Sp	$1.5 \times 1.2 \times 2.0$	Up to 5 M	Yes	Non specified gap ^d	No
[26]	Sp	$7.7 \times 7.7 \times 11.2$	Up to 45.7 M	Yes	No ground	Yes

^aSp = spoked; a-Sp = aero-spoked wheels (tri-spoke, four-spoke and five-spoke wheels); disc = disc or lenticular wheels.^bDomain size provided in wheel diameters by the authors. Dimensions in this table are calculated assuming a wheel diameter of 0.7 m.^cSize not provided.^dThe wheel/ground contact modeling is not clearly stated, but implied from pictures available in the paper.^eThe WT tests used for the CFD validation were only performed with a static wheel. The CFD simulations were performed for both static and rotating wheels.**Fig. 1.** Step size used to model the wheel/ground contact for a car wheel in side view (a) and bottom view (b), and for a bicycle wheel in bottom view (c). Source: Fig. 1b is adapted from [28] and it is reproduced with permission.

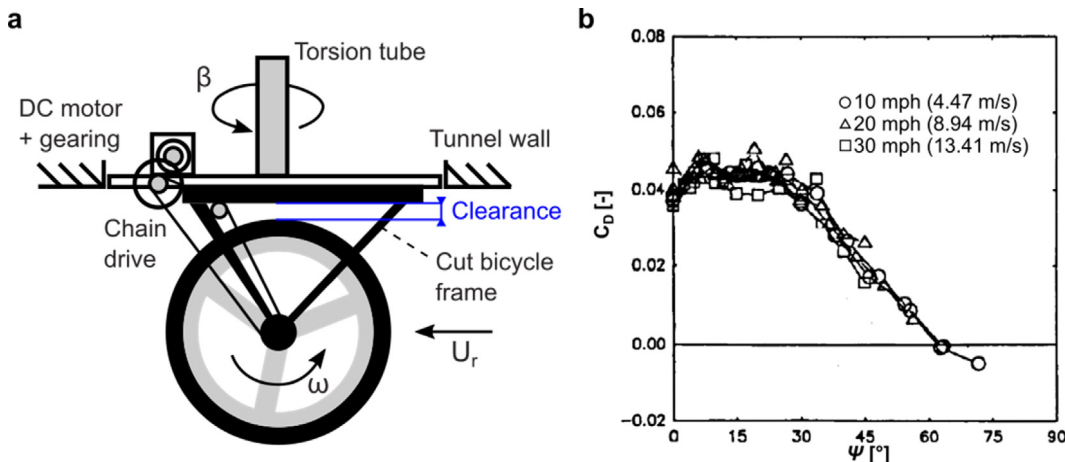


Fig. 2. (a) Wind tunnel setup of experiments by Greenwell et al. [8]. (b) Drag coefficient of the Campagnolo Shamal rear wheel for different yaw angles ψ and wind speed U_g [8].

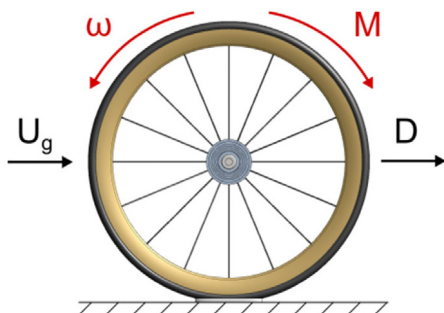


Fig. 3. Drag (D) and rotational moment (M) definitions when the wheel is moving forward at a speed U_g and rotating at a rotational speed ω in zero wind conditions.

3. CFD simulations: settings and parameters

3.1. Wheel geometry

The wheel selected in this study is the Campagnolo Shamal rear wheel used in the WT tests by Greenwell et al. [8] (Fig. 4b). This wheel is selected here because the rim and hub shapes are available in the Campagnolo 1996 catalogue (Fig. 4a,d) [45]. The wheel is equipped with a 8 gears cassette. The exact size of the sprockets is not provided by Greenwell et al. [8], therefore a 13/14/16/18/20/22/25/28 gear set was assumed, which was a combination actually available in those years [46]. The gears' shape is approximated by cylinders of diameter equal to the primitive diameter of each sprocket and a width of 2 mm. The interspace between two gears is filled by extruding the volume of the smaller of the two consecutive gears. The spoke shape is also not specified in [8], therefore it is approximated by a rectangular cross-section, similar to a previous study [26]. Greenwell et al. [8] stated that a high pressure tire was used for the Campagnolo Shamal wheel, rather than the tubular tire used for the other wheels tested: "HED 24-spoke wheel [...] is fitted with a narrow section tubular tire (as opposed to a high-pressure "HP" tire)" [8]. Because the HP tire is wider than the tubular tires used by Greenwell et al. [8], a tire of 23 mm width is taken in this study, and its shape is approximated by a 23 mm diameter circumference fitted in the rim (Fig. 4c).

3.1.1. Wheel/ground contact modeling

Two approaches are used to model the wheel/ground contact: (i) the wheel is displaced from the ground (Fig. 5a); and (ii) the wheel is in contact with the ground (Fig. 5b). In the first approach, the wheel is not physically in contact with the ground, with a minimum distance or clearance "c". While this is a commonly adopted approach in CFD studies on cycling aerodynamics [41–43], to the best of our knowledge, the effect of different clearances "c" has not yet been evaluated. Therefore, in the present study, the value of "c" is varied from 5 mm to 100 mm (Fig. 5a). In addition a case without the ground ($c = \infty$) is also considered. In the second approach, a horizontal plane at height "s" from the ground is used to cut the tire geometry, so that a flat patch is created at the bottom of the wheel. This patch is then extruded down until the ground, creating a solid volume or "step" between the tire and the ground (Figs. 1b, 5b). In the present study, the value of "s" is varied between 2.5 mm and 15 mm (Fig. 5b). Note that not only the height "s" varies, but also the length and width of the step, as a larger portion of the tire is cut when the cutting plane is moved farther from the ground, as shown in Fig. 1c. A similar approach using a step is already employed in car aerodynamics (e.g. [27,28]).

3.2. Computational domain

Two computational domains are used in this study: (i) a WT based domain and (ii) a low blockage domain. The WT based domain (Fig. 6) is divided in three regions: upstream, central and downstream. The central region has the same cross-sectional shape and size of the WT test section used by Greenwell et al. [8], i.e. an octagonal shape with test section width, height and length equal to 2.13 m, 1.52 m and 2.52 m, respectively, with lateral fillets of 0.31 m (1 ft). The wheel is located at 1.1 m distance from the beginning of the central region and it is elevated from the ground to resemble the experimental conditions. Because the distance of the wheel from the WT ceiling was not provided by Greenwell et al. [8], it is supposed to be equal to 0.05 m based on the drawing in [8]; see Fig. 2a. The cross-sectional shape of the upstream and downstream regions is the same as in the central part of the WT test section, however the choice of their length follows the CFD best practice guidelines for wind flow in the urban environment [47–50] and automotive external aerodynamics [51]: the distance between the object under analysis and the inlet should be at least 5 times the object reference height, whereas a distance of at least 10 times the reference height

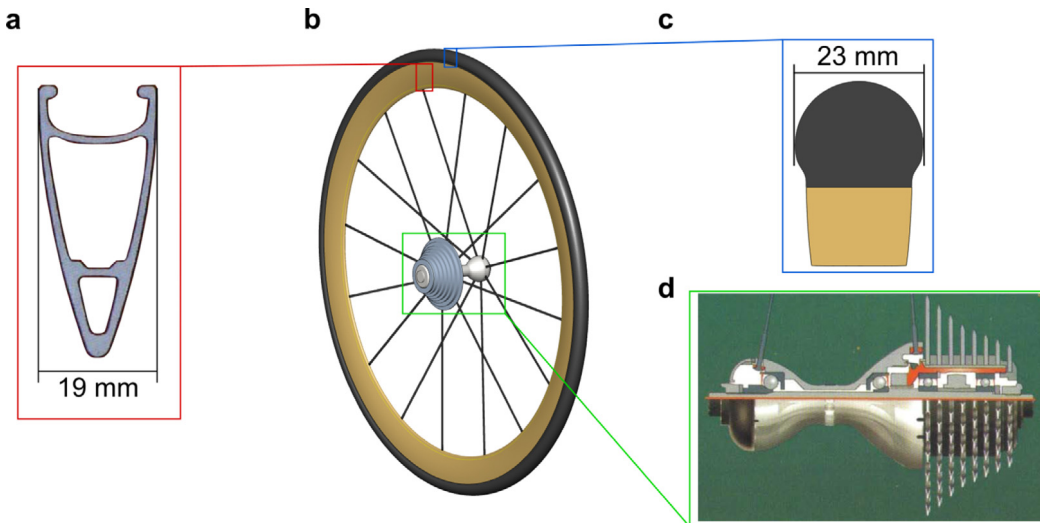


Fig. 4. Campagnolo Shamal rear wheel: (a) rim profile [45]; (b) computational geometry of the Campagnolo Shamal rear wheel; (c) tire profile; (d) hub [46]. Source: Fig. 2a and d are reproduced with permission from Campagnolo.

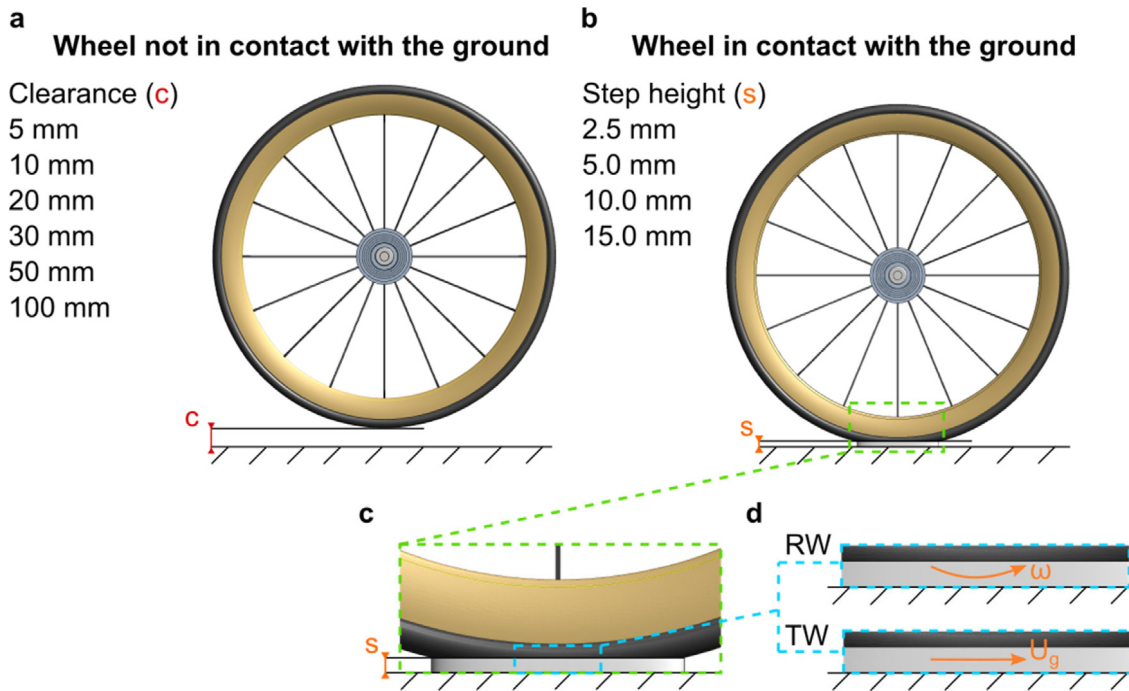


Fig. 5. (a) Definition of the clearance “*c*” between wheel and ground when they are not in contact; (b) definition of the step height “*s*”, where the step replaces the contact patch when the wheel is in contact with the ground; (c) zoomed view of the step used in the wheel/ground contact; (d) two different boundary conditions are tested on the step; rotating wall (RW) and translating wall (TW).

should be present between the object and the outlet face. In this study, the reference height is chosen to be the wheel diameter, \varnothing , therefore $5\varnothing$ and $10\varnothing$ distances are present between the wheel and the inlet and outlet, respectively. Therefore, the upstream and downstream regions are created by extending the central region front and rear faces. The resulting blockage ratio is 0.7% when the wheel is aligned with the flow.

In the “low blockage” computational domain (Fig. 7), based on the aforementioned guidelines [47–51], the distances between the wheel and the inlet, top, and lateral faces is $5\varnothing$, whereas a $10\varnothing$ spacing is present between the wheel and the outlet face. The resulting blockage ratio is smaller than 0.1% when the wheel

is aligned with the flow. When using this domain, the wheel can be either in touch with the ground or not.

3.3. Boundary conditions

For the WT based domain, a uniform velocity (U_g) and turbulence intensity ($TI = 0.5\%$) are imposed at the inlet boundary in line with the WT experiments. The inlet specific dissipation rate ω , is computed from the turbulence intensity and the hydraulic diameter, the latter set to 1.75 m, accordingly to the WT cross-sectional shape used in [8] and the equation $D_H = 4A_f/p_f$, where A_f and p_f are the frontal area and perimeter of the WT test section. Zero static gauge pressure is imposed at the domain

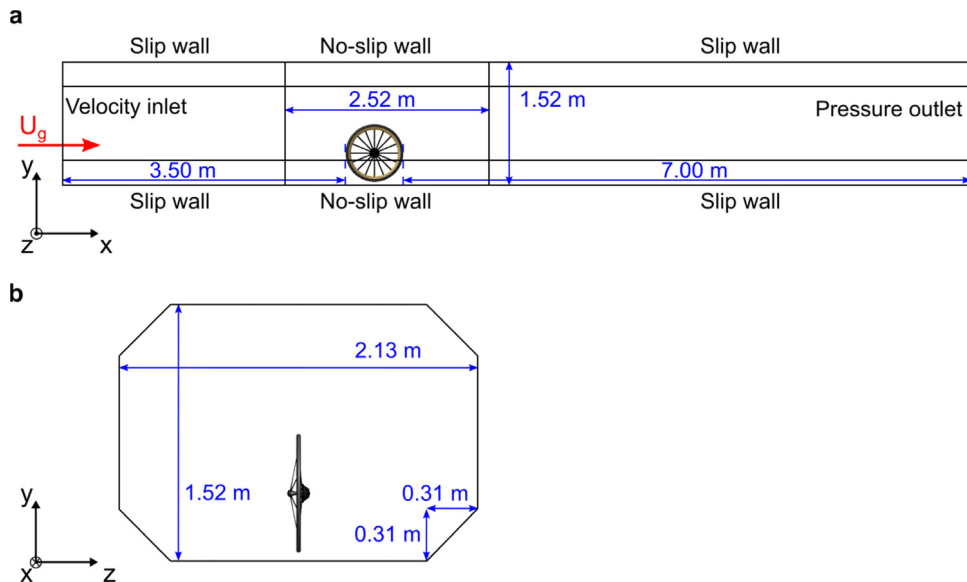


Fig. 6. Computational domain based on the wind tunnel test-section of [8]: (a) side view; (b) front view.

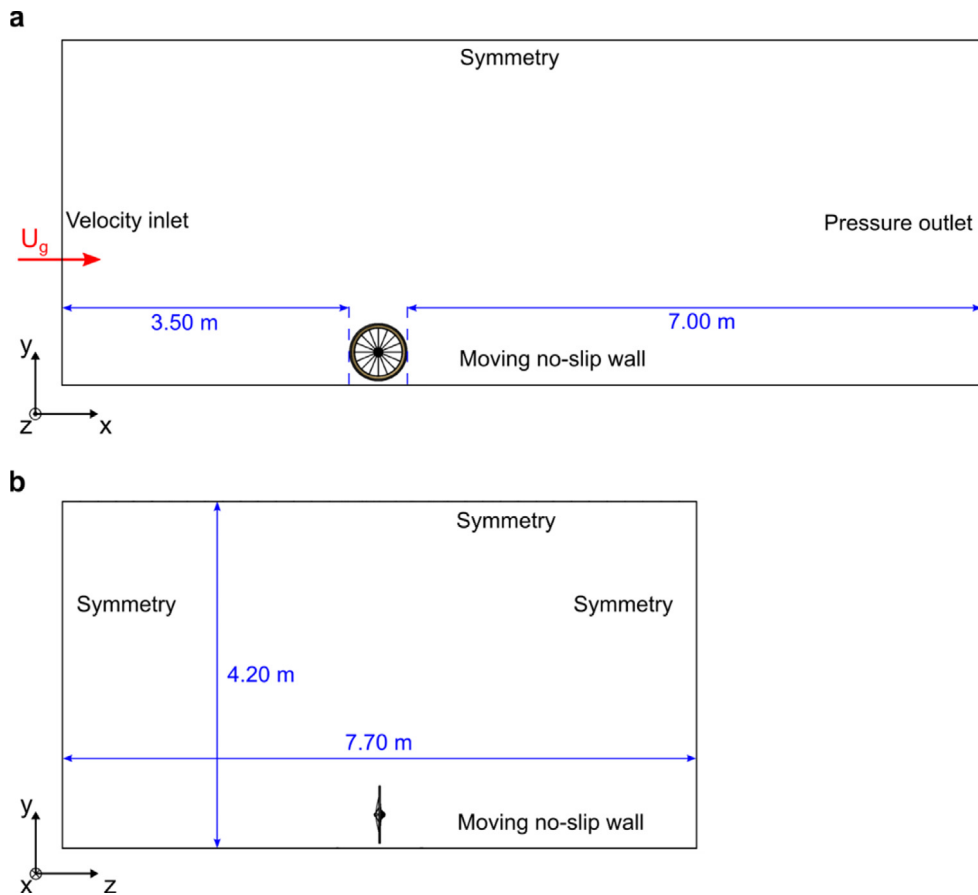


Fig. 7. ‘Low blockage’ computational domain used for the wheel/ground contact study: (a) side view; and (b) front view.

outlet. The no-slip boundary condition is applied at the lateral, top and bottom faces of the central fluid region in the WT based domain (Fig. 6), whereas the slip wall boundary condition is applied on all the side walls in the upstream and downstream fluid regions, located before and after the central fluid region, respectively.

For the low-blockage domain, the top and lateral faces of the open domain (Fig. 7) have a symmetry boundary condition applied on, whereas a translating wall boundary condition, called moving ground, is applied on the ground surface with speed U_g , direction parallel to the wheel and zero roughness. The other boundary conditions are identical to those for the WT based domain.

3.3.1. Wheel rotation and MRF shape

The wheel rotation is modeled using the hybrid MRF-RW approach, where the moving reference frame approach (MRF) and the rotating wall (RW) are combined together: the MRF approach is used inside a volume covering the spokes, the inner rim, inner hub and inner gears, whereas the RW boundary condition is applied on the outer rim, outer hub, outer gears and tire. This approach was previously validated [26] with WT tests available in literature [17]. Moreover, the motion of the contact patch is modeled either by a RW boundary condition or by a translating wall (TW) boundary condition (Fig. 5d). A cylindrical interface is present between the MRF fluid region and the external fluid region (Fig. 8a, b). Inside this interface, a rotational velocity ω is imposed:

$$\omega = \frac{U_g}{r} \quad (3)$$

The size and shape of the MRF volume have a large impact on the CFD results [26]. Malizia et al. [26] suggested to use small MRF volumes with a cylindrical or rounded shape: the distance between the inner rim edge and the MRF volume should be smaller than 15 mm. In the present study a 5 mm distance is selected between the inner rim edge and the MRF volume (Fig. 8c). The width of the MRF volume is 115 mm, thus it laterally intersects the hub and the gears (Fig. 8a,d).

3.4. Computational grid

Three grids are created for the computational grid sensitivity study: a coarse, medium and fine grid. For each grid the wheel surface and the fluid volume are refined accordingly to Table 3 and shown in Figs. 9 and 10. The grids are constructed based on the guidelines by Malizia et al. [26]. The surface grid on the wheel has quad cells on the wheel spokes (Fig. 9c) and triangular cells on all the remaining wheel components – tire, rim, hub and gears – (Fig. 9b,d). The domain ground, top, inlet, outlet and lateral faces are discretized with triangular cells. The quad cells are employed to reduce the number of cells used to discretize the long and narrow spokes. These quad cells are created using the software ANSYS/Gambit, whereas all the other surfaces are discretized using the software ANSYS/Fluent Meshing 18.2. The fluid volume (Fig. 10) is discretized with a number of prism layers between 6 (coarse grid) and 18 (fine grid) on the wheel (Table 3). These prism layers are composed by wedge and hexahedral cells, which are grown from the triangular and quad surface cells, respectively. These prism layers are created using the last-ratio growth approach, where the growth ratio is computed locally and it is based on the dimension of the surface cell: the growth rate is computed such that the last cell height of the prism layer is 35% of the local surface size. The last-ratio approach is employed to ensure a smooth transition between the prism layers and the far-field grid. Prism layers are also created on the ground using an aspect ratio growth method: the aspect ratio of the first cell is set to 10, the number of layers is equal to 4 (coarse grid), 6 (medium grid) and 8 (fine grid) with a growth ratio of 1.20 (coarse and medium grid) and 1.15 (fine grid). Externally to the prism layers, the far field grid is mainly composed by tetrahedral cells, with pyramidal cells only used in the transition zone between the hexahedral cells, growth from the spokes, and the far-field tetrahedral cells. Several body of influence size functions are used upstream and downstream the wake, with a growth ratio between consecutive cells fixed to 1.20 (coarse grid), 1.15 (medium grid) and 1.125 (fine grid). The resulting total cell counts are 5.8 million, 17.9 million and 41.2 million cells for coarse, medium and fine grid, respectively (Table 3).

3.4.1. Wheel/ground contact cases

Two additional considerations are needed when building the grid for the wheel displaced from the ground and for the wheel in touch with the ground by means of a step.

When the wheel is not in touch with the ground and at small clearances “c”, the areas on the tire and the ground in close proximity need to have a similar surface grid size, to avoid sudden jumps in size between consecutive volume cells which might negatively affect both the accuracy of the solution in terms of discretization errors and might even impede convergence.

When the wheel is in touch with the ground, the use of the step enables the creation of high quality grid in this region: without the step, highly skewed cells would be present, negatively affecting the final results [33]. The step height is varied between 2.5 mm and 15 mm, and consequently also its length and width are varied (Fig. 1c). On the side faces of this step, curvature and proximity size functions [52] are used to obtain a high quality grid: a minimum cell size of 0.3 mm is set, and at least five cells are used along the step height, and the maximum normal angle between two consecutive surface cells is fixed to 10° [52].

3.5. Computational settings

The commercial CFD code ANSYS/Fluent 18.2 is used to perform the simulations. The 3D RANS equations are solved with the $k-\omega$ SST turbulence model for closure. The selection of this turbulence model is based on previous studies on cycling aerodynamics [26,39,53–56]. Pressure–velocity coupling is performed with the Coupled algorithm, together with pseudo-transient under-relaxation. The pseudo time-step is computed following the approach for cases with rotational velocities [57]:

$$\Delta t_{pt} = \frac{0.1}{\omega} = 2.61 \cdot 10^{-3} \text{ s} \quad (4)$$

The Green–Gauss node scheme is used for the gradient evaluation, second-order interpolation is used for the pressure and second-order upwind discretization schemes are used for the remaining equations. The maximum values for the residuals are 6×10^{-4} for continuity, 7×10^{-6} for momentum, 2×10^{-3} for turbulent kinetic energy and 2×10^{-3} for the specific dissipation rate. The forces and the moment are averaged over the last 10,000 pseudo time steps from a total of 12,000.

4. Results

4.1. Grid sensitivity

The results of the grid sensitivity study are presented in Tables 4 and 5. The total values of C_D , obtained with the coarse and medium grid are 6.7% and 0.1% lower than with the fine grid, respectively. The total value of C_M is overestimated by 11.1% and 0.4% with the coarse and medium grid compared to the fine grid, respectively. However, different C_D and C_M grid sensitivity trends are noted for different wheel components. On the coarse grid, the C_D of the combined tire–rim, hub and gears is underestimated with 14.2%, 6.6% and 1.5% compared to the fine grid, respectively, whereas the C_D of the 16 spokes is overestimated with 17.6% compared to the fine grid (Table 4). The C_D results on the medium grid are in close agreement with those on the fine grid: the C_D of the combined tire–rim, and the spokes are underestimated by only 0.2% and 1.7%, respectively; whereas the C_D values of the hub and the gears are overestimated by 1.1% and 1.3%, respectively.

The hub and the gears provide almost no contribution to C_M (Table 5). Therefore the total C_M is only influenced by the combined tire–rim and by the 16 spokes, each of which have a similar contribution to the total C_M : about 53% and 47% for the combined

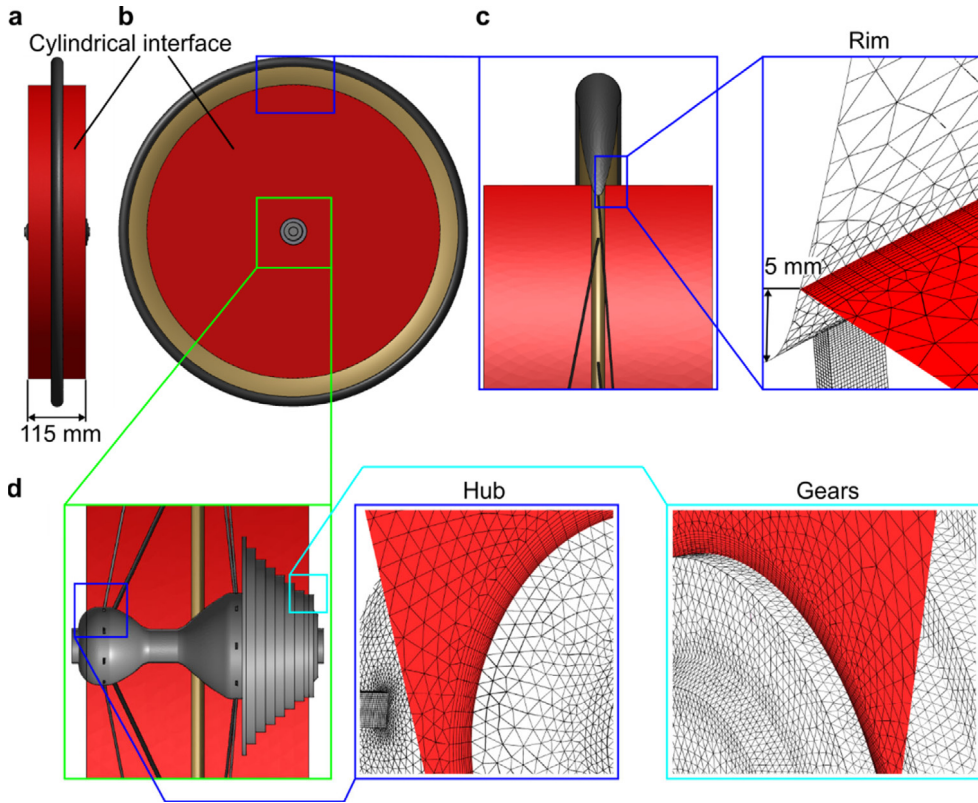


Fig. 8. The MRF-RW rotational model (combination of moving reference frame – MRF – and rotating wall – RW – approaches) is applied on the wheel. The MRF volume is shown in red, in (a) front view; (b) side view; (c) close view at the intersection between the MRF volume and the rim, and (d) close view at the intersection between the MRF volume, the hub and gears.

Table 3
Surface and volume grid details of the three grids in the grid sensitivity study.

	Surface						Volume		
	Tire	Rim	Spokes	Hub	Gears	Total	y_1 [mm]	# layers	Total
Coarse	47 k	93 k	38 k	15 k	25 k	218 k	0.150	6	5.8 M
Medium	128 k	175 k	187 k	38 k	56 k	584 k	0.080	12	17.9 M
Fine	202 k	319 k	305 k	60 k	81 k	967 k	0.025	18	41.2 M

tire-rim and the 16 spokes, respectively, on the fine grid. On the coarse grid, the C_M is overestimated for both the combined tire-rim and for the spokes by 7.5% and 15.2%, respectively, compared to the fine grid. On the medium grid, the C_M is +4.4% and -4.0% for the combined tire-rim and spokes, respectively, compared to the fine grid. However, these differences compensate each other and the total C_M of the medium grid case is only slightly larger (+0.4%) than the C_M of the fine grid.

Despite the somewhat lesser agreement of the C_M for each wheel component between the medium and fine grids, the medium grid is retained for the following analyzes since the rotational moment has a lower impact (29%) on the total power required to move the wheel compared to the aerodynamic drag (71%), for the wheel under analysis.

4.2. CFD Validation

The CFD validation is based on the WT results by Greenwell et al. [8] for the Campagnolo Shamal rear wheel. The CFD simulations are performed for the ground speeds U_g equal to 4.47, 8.94 and 13.41 m/s at 0° yaw angle. The wheel support used in the WT tests, consisting of the rear section of a cut bicycle frame in [8], is not included in the CFD simulations since its shape and dimensions are unknown. Note that the drag coefficient results, C_D , of Greenwell et al. [8] are reported here with the

minimum and maximum values, because it is not possible to clearly extract a single value from Fig. 2b. The CFD results and the WT results (where available) are presented in Table 6. The minimum C_D is computed for the case with the highest ground velocity (13.41 m/s), whereas a 9.9% and 6.8% higher drag are computed for the cases with 4.47 m/s and 8.94 m/s ground speed, respectively. The C_D values computed for the three different ground speeds lie within the range of minimum and maximum C_D values measured by [8], with the only exception of C_D for $U_g = 13.41$ m/s, where the computed C_D slightly underestimates the minimum measured C_D . A similar C_M value is computed for the cases with ground velocity equal to 13.41 m/s and 8.94 m/s, with a slightly higher C_M value (+7.9%) for ground velocity of 4.47 m/s. Note that C_M is not measured in the WT tests of [8].

Moreover, C_D and C_M are 3.5% and 0.7% higher in the CFD simulations performed with the WT based domain at $U_g = 13.41$ m/s compared to the results obtained with the low-blockage domain, respectively. This indicates a clear influence of the WT walls on the results.

4.3. Wheel/ground contact

Three cases are considered: (i) no ground present; (ii) ground present and wheel displaced from the ground with clearance “c”; and (iii) ground present and wheel in contact with the ground

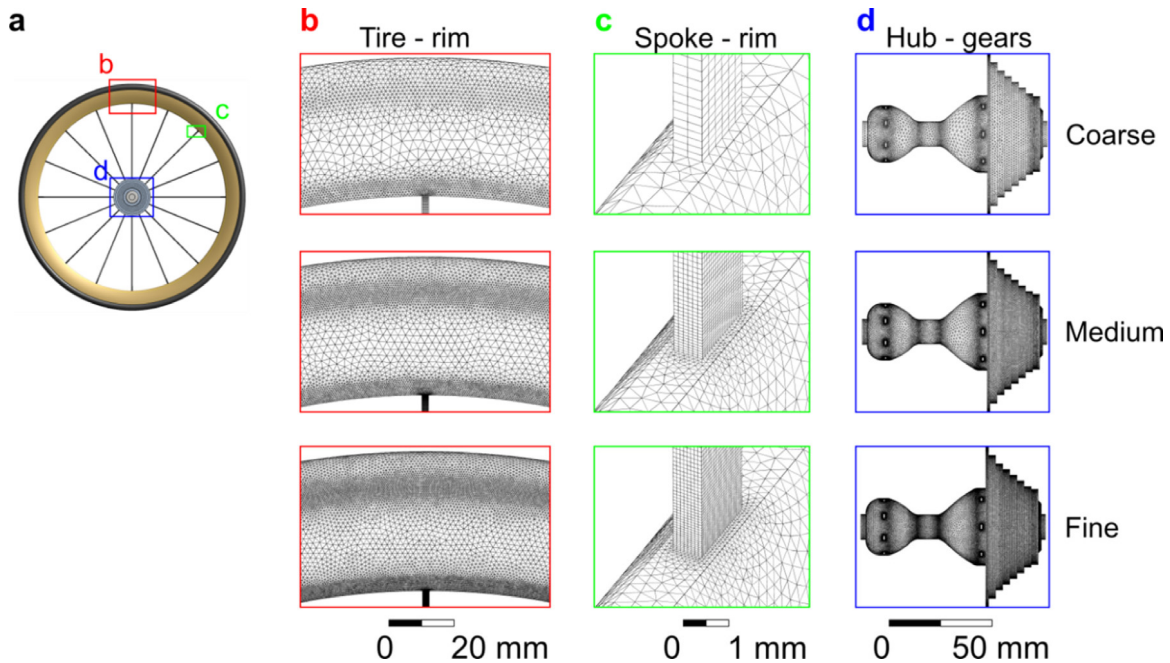


Fig. 9. Three surface grids – coarse, medium and fine – for the grid sensitivity study. (a) Wheel in side view with boxes indicating the areas for which close-ups of the grid are shown on: (b) tire-rim; (c) intersection between spoke and rim; (d) hub and gears.

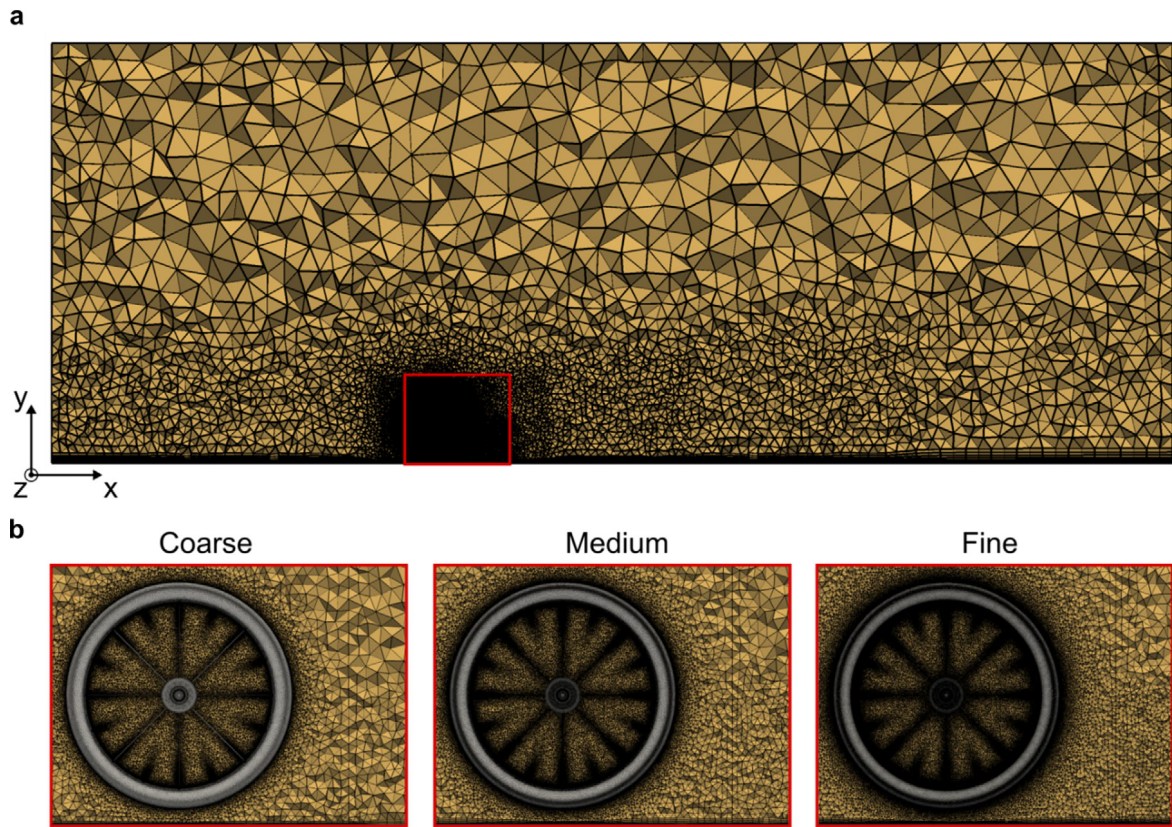


Fig. 10. (a) Volume grid in the wheel center plane $z = 0$, where the region near the wheel is highlighted in red. (b) Close views of the surface grid on the wheel surface and volume grid in the wheel center plane $z = 0$ for coarse, medium and fine grid.

by a step with height “ s ”. The parameters “ c ” and step heights “ s ” are varied to assess the sensitivity of the CFD results to these quantities. Note that case (i) resembles case (ii) with $c =$

∞ , therefore these two cases are described together. The three cases are compared to each other in terms of drag, rotational moment and pressure along the tire centerline. Also additional

Table 4

Drag coefficient (C_D) results for the three grids in the grid sensitivity study. “k” is used for thousands (10^3) and “M” for millions (10^6).

	Surface grid [# cells]	Volume grid [# cells]	y^+ [-]	C_D [-]				
				Tire & Rim	Spokes	Hub	Gears	Total
Coarse	218 k	5.8 M	4.7	0.01759	0.00640	0.00409	0.00393	0.03201
Medium	584 k	17.9 M	2.6	0.02046	0.00535	0.00443	0.00404	0.03428
Fine	967 k	41.2 M	0.8	0.02050	0.00544	0.00438	0.00399	0.03431

Table 5

Rotational moment coefficient (C_M) results for the three grids in the grid sensitivity study. “k” is used for thousands (10^3) and “M” for millions (10^6).

	Surface grid [# cells]	Volume grid [# cells]	y^+ [-]	C_M [-]				
				Tire & Rim	Spokes	Hub	Gears	Total
Coarse	218 k	5.8 M	4.7	0.00790	0.00750	0.00000	0.00001	0.01541
Medium	584 k	17.9 M	2.6	0.00767	0.00625	0.00000	0.00001	0.01393
Fine	967 k	41.2 M	0.8	0.00735	0.00651	0.00000	0.00001	0.01387

Table 6

Computed drag (C_D) and rotational moment (C_M) coefficients compared to the wind tunnel results of [8]. Greenwell et al. [8] did not provide the accuracy of their WT experiments. For this table, the results are reported in line with the stated accuracy of the WT experiments by Tew and Sayers [17] on isolated wheels (± 0.0005).

	U_g [m/s]	C_D [-]	C_M [-]
CFD	4.47	0.0390	0.0151
CFD	8.94	0.0379	0.0141
CFD	13.41	0.0355	0.0140
WT _{min}	4.47 to 13.41	0.0356	n.a.
WT _{max}	4.47 to 13.41	0.0405	n.a.

information about the flow field and C_p distributions on the entire wheel, ground and on transversal planes in the wheel's wake are presented.

4.3.1. Wheel displaced from the ground: sensitivity to clearance “c”

Seven values for “c” are tested, one where the ground is neglected and six where “c” ranges from 5 mm to 100 mm. The results are showed in Table 7. Considering the case with the smallest clearance from the ground ($c = 5$ mm) as reference, +1.7% and +2.1% larger C_D and C_M are found for the case with $c = 100$ mm, respectively. These C_D and C_M differences reduce to +0.7% and +1.0% for the case with $c = 50$ mm, respectively, and to -0.1% and +0.2% for the $c = 20$ mm case. For the case without the ground, +1.0% and +2.0% differences for C_D and C_M are found compared to the case with smallest “c” distance, respectively. Therefore the sensitivity of the distance between the ground and the wheel to the C_D and C_M is found to be small for all the distances tested, with a negligible impact for $c \leq 20$ mm.

However, the pressure coefficient plot (Fig. 11b) along the tire centerline (Fig. 11a) shows a different pressure distribution for the different cases with and without the ground. The pressure coefficient, C_p , is defined as:

$$C_p = \frac{P - P_\infty}{0.5 \rho U_r^2} \quad (5)$$

where P and P_∞ are the static pressure at the point of interest and the unperturbed static pressure at the inlet, respectively. The largest C_p differences are found in the lower half and back of the wheel, between 50° and 200°. Moving the wheel closer to the ground (smaller “c”), the overpressure at around $\theta = 90^\circ$ (P_1 in Fig. 11b) increases with a maximum value of 0.62 and 0.84 for the cases with $c = 100$ mm and $c = 5$ mm, respectively, and of 0.51 for the case without the ground. Moreover, the angle at which this maximum value is computed moves from about 83° (no ground case) to 86° ($c = 100$ mm) and to about 94° ($c = 5$ mm). After

Table 7

Drag (C_D) and rotational moment (C_M) coefficients computed for different distances “c” of the wheel from the ground when they are not in contact.

Distance c [mm]	C_D [-]	C_M [-]
5	0.03405	0.01379
10	0.03407	0.01374
20	0.03402	0.01382
30	0.03411	0.01387
50	0.03428	0.01393
100	0.03463	0.01408
No ground	0.03440	0.01407

this peak, a local minimum (Di_1) followed by one additional local maximum (P_2) and minimum (Di_2) is found for the $c = 5$ mm case at around 125°, 140° and 160°, respectively. Similarly to the first peak at around 90°, the local maximum and local minimum shift backwards several degrees on the wheel – thus at larger θ – when decreasing the distance “c” from the ground. In addition, the local C_p peak P_2 value increases and the local C_p dips, Di_1 and Di_2 , became less negative when decreasing “c”. Additional insights on this C_p behavior are presented in Section 4.3.4 and shown in Figs. 15 and 16. Conversely, no significant C_p differences are noted in the upper-front part of the wheel.

4.3.2. Wheel in contact with the ground: sensitivity to step height “s” and step boundary condition

The wheel/ground contact is modeled here using a step with four different heights, ranging from 2.5 mm to 15.0 mm, and with two different boundary conditions imposed on the step, i.e. rotating wall (RW) and translating wall (TW). The results are shown in Table 8. Using as reference the case with the smallest step height $s = 2.5$ mm, the C_D and C_M differences might be considered negligible ($\leq 0.4\%$) when using the step heights of 5 mm and 10 mm for both boundary conditions. For the largest step height considered, 15 mm, a 0.7% and 0.6% larger C_D is computed compared to the $s = 2.5$ mm case when using the RW and TW boundary conditions, respectively. The value of C_M is -0.6% and -0.4% lower for $s = 15$ mm than for $s = 2.5$ mm when using the RW and TW boundary conditions, respectively.

Fig. 11c,d show C_p along the tire centerline for the cases with RW and TW boundary conditions imposed on the tire step. A $C_p > 1$ is found in front of the step for both cases ($\theta \sim 90^\circ$). This behavior has already been observed in both WT tests (e.g. [31,58]) and CFD simulations (e.g. [27–29,33,35]) of car wheels. The $C_p > 1$ was explained by the “jetting” effect in front of the wheel [31,33]: the tire – where a rotating wall boundary condition is applied – is approaching the moving ground near the contact patch, causing an increase in C_p beyond the value of one, where a value of one

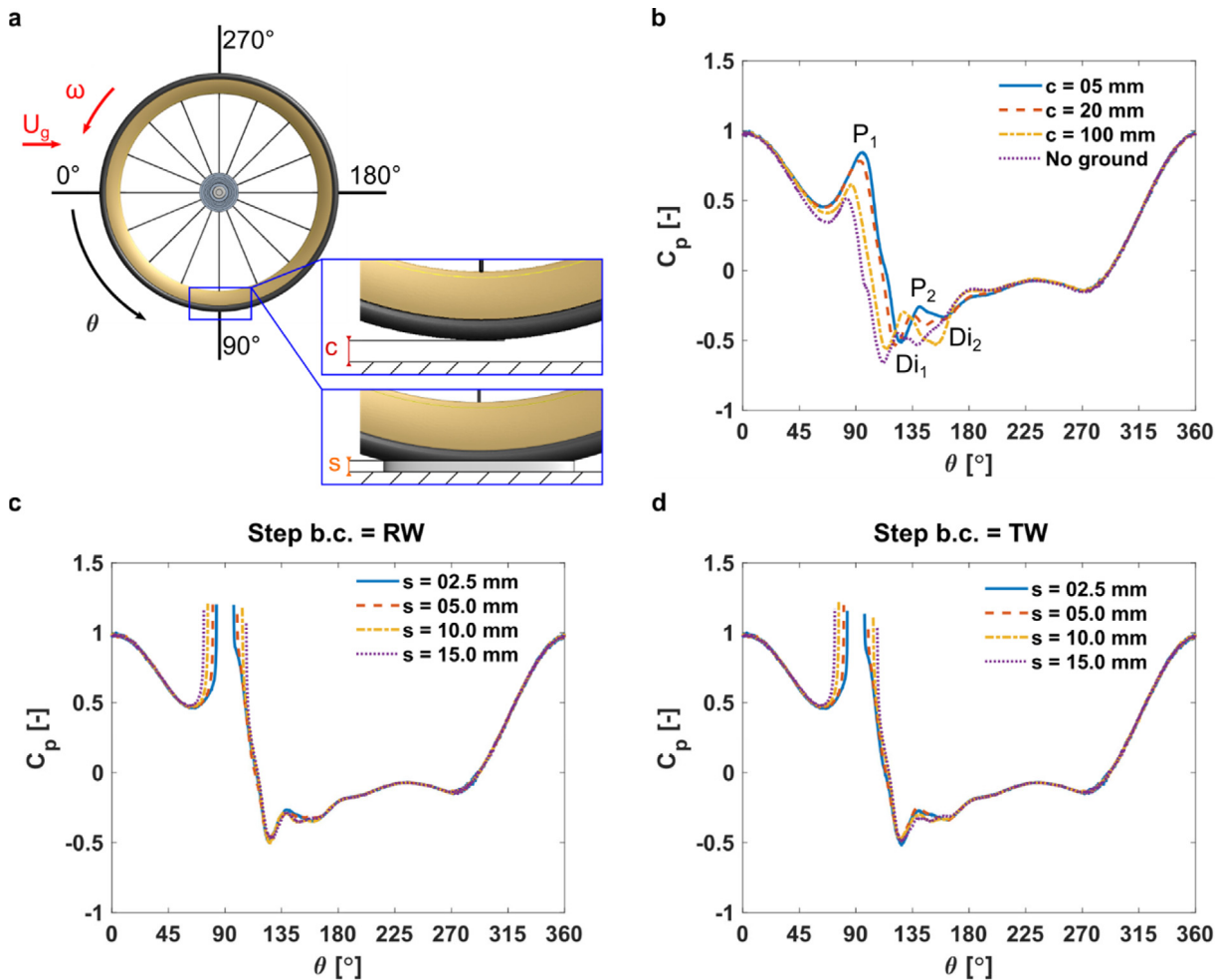


Fig. 11. (a) Definition of ground clearance “ c ” and step height “ s ”; (b) pressure coefficient (C_p) distribution along the exterior tire centerline for different “ c ” and the case with no ground; (c) C_p distribution along exterior tire centerline for different “ s ” with a rotating wall boundary condition (RW) applied on the step; (d) Same as (c) but with a translating wall boundary condition (TW).

corresponds to the stagnation value. Conversely, after the contact point the rotating wheel and the moving ground move away each other, causing a drop in the C_p .

The main C_p differences are localized near the step, with the C_p rise and fall occurring at lower and higher θ angles for larger step heights, respectively: this is caused by the increase of the step length when its height “ s ” is increased (Fig. 1c). Nevertheless, the peak value is almost constant for all the cases analyzed, with values around 1.2. Similar to the case with the wheel displaced from the ground, also in the CFD simulations with the step, two local dips and one local peak are found at θ between 120° and 160°, however their magnitude and θ location are not influenced by the step height: likely these dips and peaks are mainly influenced by the overall distance between the ground and the wheel, which is independent from the step height.

Fig. 12 shows the C_p along the step front centerline, for both RW (Fig. 12b) and TW (Fig. 12c) cases and all step heights, where the y -coordinate is made dimensionless by the step height for each case. The C_p exhibits a very similar behavior for each step height and boundary condition, with slightly smaller C_p along the height of the step for the $s = 2.5\text{ mm}$ case compared to the cases with larger s . Note that the C_p values along the step height are almost 1 with the only exceptions at the intersection between the step and the tire, and between the step and the ground, where C_p of about 1.2 and 1.5 are computed, respectively. The slightly

Table 8

Drag (C_D) and rotational moment (C_M) coefficients computed for different “ s ” when the wheel is in contact with the ground. Two boundary conditions are considered for the step: rotating wall (RW) and translating wall (TW).

Step height	RW		TW	
	C_D [-]	C_M [-]	C_D [-]	C_M [-]
2.5	0.03379 (ref.)	0.01382	0.03381	0.01379
5.0	0.03375	0.01384	0.03378	0.01385
10.0	0.03385	0.01384	0.03383	0.01381
15.0	0.03399	0.01372	0.03402	0.01373

lower values at the middle height of the step for the case with the smallest height tested, 2.5 mm, might be caused either by the fewer number of cells (about 6) along the step height for $s = 2.5\text{ mm}$ – thus caused by the spatial discretization – or by the smaller space available for the air to flow around the step – thus caused by the physics of the problem. However, due to the very limited impact of this difference, it is considered not necessary to further investigate it.

4.3.3. Wheel/ground contact modeling: comparison between the different approaches

The results obtained with the smallest ground distance ($c = 5.0\text{ mm}$) and the smallest step height ($s = 2.5\text{ mm}$) for both

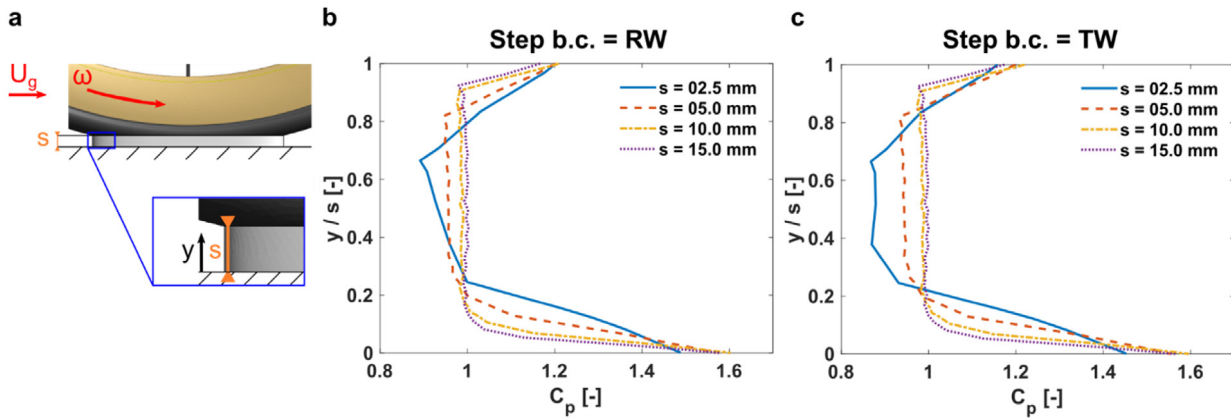


Fig. 12. (a) Definition of the step height s ; (b) pressure coefficient C_p distribution along the step height with rotating wall boundary condition (RW) applied on the step; (c) same as (b) but with translating wall boundary condition (TW).

RW and TW boundary conditions are here compared each other and to the case without the ground. The C_D for $c = 5.0$ mm, $s = 2.5$ mm using the RW and TW boundary conditions are -1.0% , -1.8% and 1.7% lower than the case without the ground, respectively, whereas the C_M is -2.0% , -1.8% and -2.0% lower than the case without the ground, respectively.

The C_p differences between the cases with the ground and the case without the ground are located between $\theta = 45^\circ$ and 180° (Fig. 13b). A smaller C_p peak at smaller θ is found for the case without the ground, in addition to the more negative C_p dips and secondary C_p peak. The C_p differences between the cases with the ground and without are almost negligible in the upper and front part of the wheel ($\theta < 45^\circ$ and $\theta > 180^\circ$).

Considering only the three cases with the ground present, the C_p differences are mainly located at around $\theta = 90^\circ$ (Fig. 13b), where the geometry of the two modeling approaches is different and the wheel is closest to the ground (Fig. 13a). When the wheel is displaced from the ground (Fig. 14b), the air can pass below the wheel causing the absence of a zone with $C_p > 1$. Nevertheless, a C_p bump is still observed at around $\theta = 90^\circ$ for the case with clearance: the air flowing between the wheel and the ground is decelerating – as shown in Fig. 14b – thus causing the C_p increase near $\theta = 90^\circ$ (Fig. 13b). It is argued that the lack of an accelerating flow between the cycling wheel and the ground is due to the narrow width of the tire and the resulting high flow resistance, which facilitates the air to flow around the tire rather than below it. After $\theta \sim 100^\circ$, the C_p curve for the case $c = 5.0$ mm has no noticeable differences from the C_p curves for either RW or TW boundary conditions for $s = 2.5$ mm.

Fig. 14c,d shows the vector plots of the 2D velocity components in a vertical centerplane and contours colored by the normalized streamwise velocity component in the same vertical plane near the step for both RW and TW boundary conditions, respectively. The figures show a low value in front of the step, where also a small area of stagnating and reverse flow is present. These observations are in line with the C_p values plotted along the step height in front of the wheel (Fig. 12b,c), where a C_p smaller than one is found at the middle height of the step for $s = 2.5$ mm.

4.3.4. Flow field visualizations

To further elucidate the flow behavior around the wheel and near the ground – when present – and to clarify the variations of C_p around the tire circumference, Fig. 15 provides additional isosurfaces and contours of C_p for the three cases analyzed, no ground, wheel/ground contact modeled with a clearance, wheel/ground contact modeled with a step and RW boundary condition, whereas Fig. 16 provides contours of C_p and vector

fields to observe more in detail the flow behavior for the case with ground and the wheel/ground/contact modeled with a step.

Fig. 15a shows the contours of C_p in the wheel centerplane for the case without the ground. The flow near the front-bottom section of the tire and rim is characterized by a $C_p > 0$, whereas the flow near the rear-bottom section of the tire and rim has a negative C_p . The negative C_p near this wheel region is connected to a negative C_p flow originated in the wake of the hub and gears, see also Fig. 15b, where the isosurfaces of $C_p = -0.3$ around the wheel are shown in gray color. The main isosurfaces of $C_p = -0.3$ are almost symmetrical leaving the hub and gears, where they are generated, and approach the rear-bottom regions of the rim and tire and continue in the wheel's wake, mainly in the downstream direction. In addition a horizontal plane located 0.10 m below the wheel is displayed in Fig. 15b, showing that the $C_p = -0.3$ isosurfaces are mainly located above this plane. Fig. 15c and d show the same isosurfaces of $C_p = -0.3$ around the wheel for $c = 5.0$ mm and for $s = 2.5$ mm and RW boundary condition, respectively. The isosurfaces are again almost symmetrical leaving the hub and gears and approach the bottom rear regions of the rim and tire at $\theta = 125^\circ$ and 170° , where the local C_p peaks and dips at the tire centerline are found, as shown in Fig. 11. Once the negative pressure flow reaches the ground, the two main isosurfaces not only move downstream but also move in the spanwise direction, differently to the case with no ground. This highlights the complex flow dynamics around a cycling spoked wheel and the ground. Fig. 15b,c,d also show the C_p distribution on the entire wheel and ground. The front section of the tire, front section of the hub and gears, and the bottom of tire and rim (at around $\theta = 90^\circ$) are characterized by high C_p . In addition, a high C_p is also present at the ground near the clearance or near the step (Fig. 15c,d). Note that also an additional high C_p region is present on the ground in the wake of the wheel. This high C_p region is located in between two regions of low C_p which are caused by the low pressure wake created at the hub and gears. This low pressure wake reaches first the tire and the rim, at $125^\circ < \theta < 170^\circ$, and then the ground.

Fig. 16a shows C_p contour plots in the wheel centerplane and Fig. 16b-g show vector and C_p contour plots in six lateral vertical planes located in at distances of $x = -1/4\theta$, 0 , $+1/4\theta$, $+5/8\theta$, $+3/4\theta$ and $+\theta$ from the hub center for the $s = 2.5$ mm case. The vector plots indicate a clear downwash in the wheel's wake between the two flow regions with counter-rotating flow with low pressure, with air moving outwards when reaching the ground, laterally from the high to the low pressure zones. These two low pressure flow zones also move spanwise, as also shown in Fig. 15c,d.

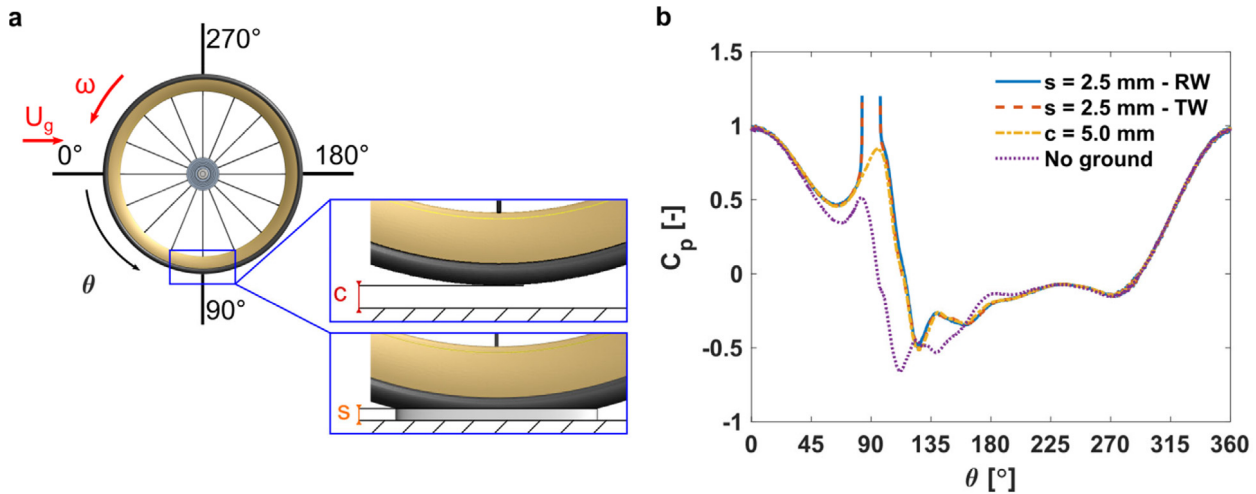


Fig. 13. (a) Definition of distances “ c ” and step heights “ s ” for the cases of wheel not in contact and wheel in contact with the ground, respectively. (b) Comparison of C_p values along the exterior centerline for three different types of ground contact modeling and for the case with no ground.

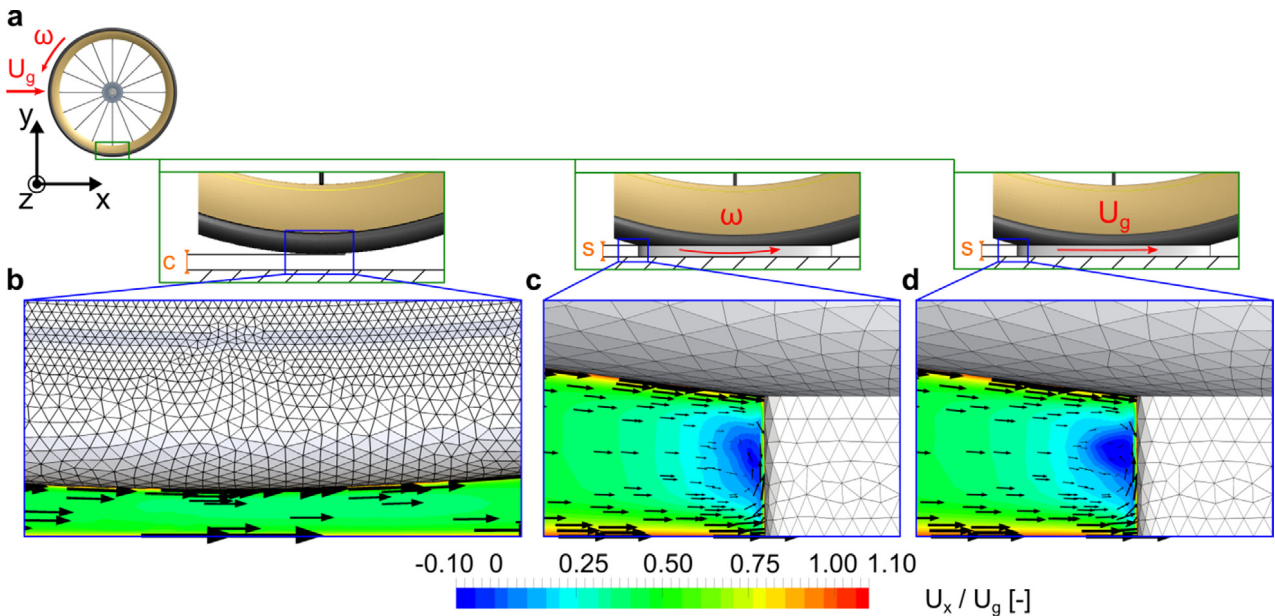


Fig. 14. (a) Definition of distance “ c ” and step height “ s ” for the cases of wheel not in contact and wheel in contact with the ground, respectively. (b-d) Contours of wind speed ratio in a vertical centerplane for (b) $c = 5.0 \text{ mm}$; (c) $s = 2.5 \text{ mm}$ and rotating wall boundary condition; and (d) $s = 2.5 \text{ mm}$ and translating wall boundary condition.

5. Limitations and future work

The main limitations of this study are:

- The exact spoke and tire shapes of the wheel used in the WT tests of [8] are not provided, therefore they are approximated based on the information available [8,17]. The spoke shape was approximated with a rectangular cross-section, and the use of this approximation was already discussed in the appendix of [26]. However, being the main scope of the paper the investigation of wheel/ground contact modeling, the approximations used for the spoke and tire shapes are supposed to not compromise the findings of the paper.
- The wheel is considered in isolation from other bicycle components, similar to previous WT and CFD studies on cycling wheel aerodynamics (e.g. [20,23,26]) and similar to several studies on car wheel aerodynamics (e.g. [27–29,35]).

- Only a spoked wheel with 16 spokes is tested. The impact of the ground might be different for trispoke and disc wheels and additional studies should be conducted to investigate its impact on these types of wheels.
- The CFD validation is performed comparing the wheel drag at one yaw angle and three different speeds with WT results available in the literature [8]. To the best of our knowledge, no additional WT data, like pressure measurements on the tire and velocity measurements in the wheel's wake, are available in the literature on cycling spoked wheels, whereas present and future research would highly benefit from them.
- Scale resolving CFD simulations, e.g. URANS, SAS or LES, could provide additional insights about the impact of the wheel/ground contact modeling on spoked wheel aerodynamics. However, the RANS approach is still the main numerical approach in many aerodynamic applications [59–61], therefore this approach was chosen for the present study.

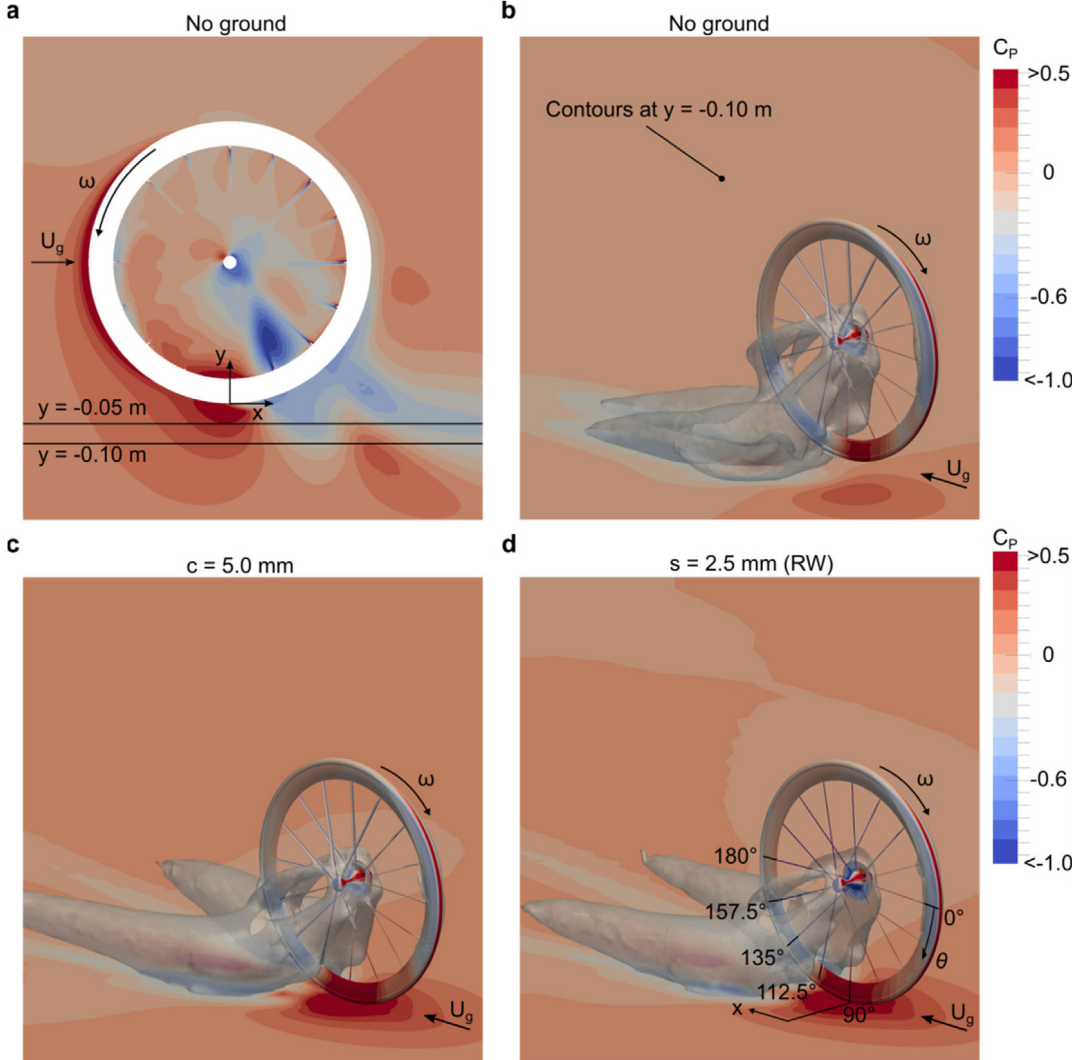


Fig. 15. (a) Contours of pressure coefficient C_p in the wheel centerplane for the case with no ground. (b) Isosurfaces of $C_p = -0.3$ (gray) together with wheel and C_p contours in a plane 0.10 m below the wheel for the case with no ground. (c,d) Same as (b) but showing the C_p contours on the ground and for (c) $c = 5.0 \text{ mm}$; and (d) $s = 2.5 \text{ mm}$ with rotating wall (RW) boundary condition.

Despite these limitations, this paper provides a first detailed quantification of the impact of the wheel/ground contact modeling on CFD simulations of cycling spoked wheels, together with flow visualizations that aid in the understanding of the complex flow behavior around this type of wheels.

The flow field visualizations indicated two large low pressure flow regions that develop after the hub and the gears and that first encounter the rear back of the wheel then the ground. This behavior suggests the presence of two counter rotating vortices leaving the hub and the gears and interacting with the bottom back of the wheel and the ground. This understanding might open room for innovations in the design of hub shapes that might optimize the wheel aerodynamics. However, note that this flow behavior is observed for only one wheel type, thus one hub shape. Future investigations should investigate different wheels (trispoke and disc) and different hub shapes, to check whether this flow behavior is present for different cycling wheels, or whether it is specific to some wheel and hub types only. In addition, the tested wheel included also the gears, which might have caused a different flow behavior compared to the one present around front wheels without the gears.

It is worth to mention that the weight of the combined cyclist-bicycle system and the tire pressure have an impact on the tire

rolling resistance and on the tire footprint size, as shown for example by Kyle [62]. In the present study, the use of a step to model the wheel ground contact was mainly incited by grid generation constraints. It is shown in Table 8 and Fig. 12 that the step size has a small influence on the aerodynamic results at zero degree yaw angle only for the largest case analyzed, with a step height equal to 15 mm and a step length equal to 203 mm. Future research should investigate the impact of the wheel/ground contact modeling on wheel aerodynamics also for cases with crosswind, thus at yaw angles larger than 0° .

Depending on the overall accuracy of the CFD simulation, the low differences in drag as a function of the step height "s" might be less significant. However, in the presence of crosswind or for cases where the interaction between the wheels, the bicycle, the cyclist body and the ground is more important, such as in hand-cycling and recumbent bicycles, these differences could be amplified. Further research is needed to investigate the influence of step height also for these types of bicycles.

CFD simulations and WT experiments are usually performed for ideally flat and uniformly rough ground surfaces. While this assumption is considered appropriate for velodromes, it might be less appropriate for actual road surfaces. Further research is required to elucidate the impact of road roughness on overall

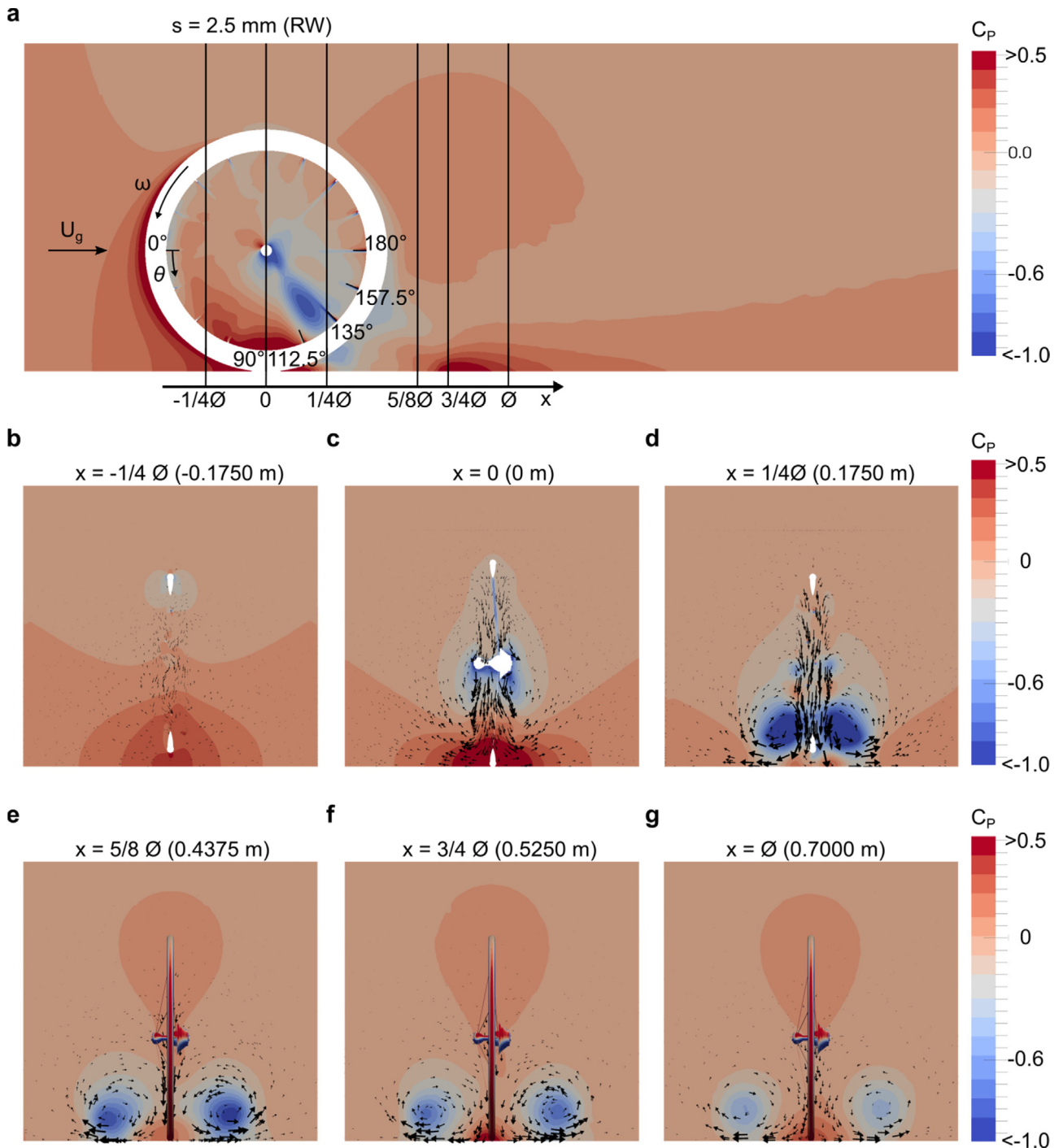


Fig. 16. (a) Contours of pressure coefficient C_p in the wheel centerplane for the case with $s = 2.5 \text{ mm}$ and rotating wall (RW) boundary condition applied on the step. (b–g) Vector plots and contours of C_p in lateral vertical planes at six streamwise distances from the hub center $x =$ (b) $-1/4\varnothing$; (c) 0; (d) $+1/4\varnothing$; (e) $+5/8\varnothing$; (f) $+3/4\varnothing$; and (g) $+\varnothing$, where \varnothing is the wheel diameter equal to 700 mm.

wheel performance. The same holds for the impact of lateral wheel movement on the wheel aerodynamics.

Lastly, one of the main issues in the search for high-quality experimental data for CFD validation is the lack of experimental data that have been reported in a very complete way including all relevant details that can have an impact on the target parameters. Even though the work by Greenwell et al. [8] is considered suitable for the purpose of the present paper, it would have been even better if also additional information on these measurements would have been reported, such as the wheel ground clearance,

the tire shape and all the geometrical details of the support system.

6. Summary and conclusions

The present paper systematically investigates the impact of the ground presence and the impact of the wheel/ground contact modeling on the computed forces and moments for a cycling spoked wheel and elucidates the flow behavior around this wheel for zero yaw conditions. The wheel/ground contact is modeled either with a given clearance between the tire and the ground

or with a given height of a solid contact patch (step). The flow field visualizations show that in the front section of the tire, hub and gears, a high pressure coefficient C_p is present. The inclusion of the ground in the simulations causes a large C_p peak on the wheel and on the ground near the clearance or the step, with C_p values that exceed one when the wheel/ground contact is modeled through a step. Moreover, two flow regions with negative C_p develop in the wheel's wake starting from the hub and gears and approaching first the bottom-rear regions of the rim and tire in between $\theta = 125^\circ$ and 170° , then reaching the ground. The interaction between these low pressure fluid flows and the wheel causes a C_p peak and two C_p dips along the tire centerline in the range of the above-mentioned angles. The two flow regions with low pressure are characterized by a counter-rotating flow which cause a downwash velocity in the wheel's wake and an additional high C_p region on the ground downstream the wheel. In terms of the resulting forces and moments, the main conclusions of the present paper can be summarized as follows:

- When the ground is included in the CFD simulations, a 1.0%, 1.8% and 1.7% lower drag coefficient (C_D) is found when the wheel/ground contact is modeled using a clearance of 5 mm, a step of 2.5 mm height with rotating wall (RW) boundary condition and a step with translating wall (TW) boundary condition, respectively, compared to the case without the ground.
- When the ground is included, a 2.0%, 1.8% and 2.0% lower rotational moment coefficient (C_M) is found when the wheel/ground contact is modeled using a clearance of 5 mm, a step of 2.5 mm height with RW boundary condition and a step with TW boundary condition, respectively, compared to the case without the ground.
- When the wheel/ground contact is modeled with a clearance, a maximum distance of 20 mm between the ground and wheel should be used. This will result in a difference of about -0.1% and $+0.2\%$ for the C_D and C_M compared to the case with a minimum clearance of 5.0 mm.
- When the wheel/ground contact is modeled through a step, the step height should be maximum 10 mm, and either a RW or TW boundary condition could be applied on the step. This will result in a difference of about $+0.2\%$ and 0.1% for the C_D and C_M compared to the case with a minimum step of 2.5 mm.

These results are intended to help researchers and manufacturers to perform accurate CFD simulations of wheels, isolated or combined with the rest of the bicycle, and to stimulate the design of the next generation of cycling spoked wheels.

Declaration of competing interest

The authors declare that they have no known competing financial interests or personal relationships that could have appeared to influence the work reported in this paper.

Acknowledgments

The activity presented in this paper is part of the Ph.D. research grant (dossier nr. IWT.141701) of the first author awarded by the Flemish Agency for Innovation and Entrepreneurship (VLAIO) in Belgium and also part of his work while he was afterwards appointed at Eindhoven University of Technology. The authors acknowledge the partnership with ANSYS CFD. This work was also sponsored by NWO Exact and Natural Sciences for the use of supercomputer facilities. We thank Campagnolo for the permission to reproduce Fig. 4a and Fig. 4d. The authors are also very grateful to the anonymous reviewers for their very valuable and constructive comments on this paper.

References

- [1] F. Grappe, R. Candau, A. Belli, J.D. Rouillon, Aerodynamic drag in field cycling, *Ergonomics* 40 (1997) 1299–1311.
- [2] C.R. Kyle, E.R. Burke, Improving the racing bicycle, *Mech. Eng.* (1984) 34–45.
- [3] T. Nonweiler, The air resistance of racing cyclists, 1956.
- [4] T. Defraeye, B. Blocken, E. Koninckx, P. Hespel, J. Carmeliet, Aerodynamic study of different cyclist positions: CFD analysis and full-scale wind-tunnel tests, *J. Biomech.* 43 (2010) 1262–1268.
- [5] J.C. Martin, D.L. Milliken, J.E. Cobb, K.L. McFadden, A.R. Coggan, Validation of a mathematical model for road cycling.pdf, *J. Appl. Biomed.* 14 (1998) 276–291.
- [6] P.E. di Prampero, G. Cortili, P. Mognoni, F. Saibene, Equation of motion of a cyclist, *J. Appl. Physiol.* 47 (1979) 201–206.
- [7] J.C. Martin, A.S. Gardner, M. Barras, D.T. Martin, Modeling sprint cycling using field-derived parameters and forward integration, *Med. Sci. Sports Exerc.* 38 (2006) 592–597.
- [8] D.I. Greenwell, N.J. Wood, E.K.L. Bridge, R.J. Addy, Aerodynamic characteristics of low-drag bicycle wheels, *Aeronaut. J.* 99 (1995) 109–120.
- [9] M. Allen, Tour de France bikes 2019: who's riding what? 2019, <https://www.bikeradar.com/features/pro-bike/tour-de-france-bikes/%OA> (accessed September 20, 2019).
- [10] N. Barry, D. Burton, T. Crouch, J. Sheridan, R. Luescher, Effect of crosswinds and wheel selection on the aerodynamic behavior of a cyclist, *Procedia Eng.* 34 (2012) 20–25.
- [11] M.N. Godo, D. Corson, S.M. Legensky, F.P. Manager, S. Analyst, C. Park, G. Manager, A practical analysis of unsteady flow around a bicycle wheel, fork and partial frame using CFD, 2011, pp. 1–25.
- [12] C.R. Kyle, Aero wheel performance, *Cycl. Sci.* (1995) 6–9, 20–21.
- [13] C.R. Kyle, Wind tunnel tests of bicycle wheels and helmets, *Cycl. Sci.* (1990) 27–30.
- [14] C.R. Kyle, New aero wheel tests, *Cycl. Sci.* (1991) 27–30.
- [15] C.R. Kyle, Selecting cycling equipment, in: E.R. Burke (Ed.), *High Tech Cycl.*, second ed., Human Kinetics Books, Champaign, IL, USA, 2002, pp. 1–48.
- [16] M.M. Zdravkovich, Aerodynamics of bicycle wheel and frame, *J. Wind Eng. Ind. Aerodyn.* 40 (1992) 55–70.
- [17] G.S. Tew, A.T. Sayers, Aerodynamics of yawed racing cycle wheels, *J. Wind Eng. Ind. Aerodyn.* 82 (1999) 209–222.
- [18] A.T. Sayers, P. Stanley, Drag force on rotating racing cycle wheels, *J. Wind Eng. Ind. Aerodyn.* 53 (1994) 431–440.
- [19] M. Jermy, J. Moore, M. Bloomfield, Translational and rotational aerodynamic drag of composite construction bicycle wheels, *Proc. Inst. Mech. Eng. P* 222 (2008) 91–102.
- [20] R. Crane, C. Morton, Drag and side force analysis on bicycle wheel-tire combinations, *J. Fluids Eng. Trans. ASME* 140 (2018) 1–8.
- [21] J. Knupe, D. Farmer, Aerodynamics of high performance race bicycle wheels, 2009, pp. 1–15.
- [22] M.N. Godo, D. Corson, S.M. Legensky, An aerodynamic study of bicycle wheel performance using CFD, in: 47th AIAA Aerosp. Sci. Meet. Incl. New Horizons Forum Aerosp. Expo. Vol. 12065, 2009, pp. 1–21.
- [23] M. Godo, D. Corson, S. Legensky, A comparative aerodynamic study of commercial bicycle wheels using CFD, in: 48th AIAA Aerosp. Sci. Meet. Incl. New Horizons Forum Aerosp. Expo. Vol. 35, 2010, pp. 1–31.
- [24] S.J. Karabelas, N.C. Markatos, Aerodynamics of fixed and rotating spoked cycling wheels, *J. Fluids Eng.* 134 (2012) 011102.
- [25] M. Pogni, N. Petrone, Comparison of the aerodynamic performance of five racing bicycle wheels by means of CFD calculations, *Procedia Eng.* 147 (2016) 74–80.
- [26] F. Malizia, H. Montazeri, B. Blocken, CFD simulations of spoked wheel aerodynamics in cycling: Impact of computational parameters, *J. Wind Eng. Ind. Aerodyn.* 194 (2019).
- [27] L. Axon, K. Garry, J. Howell, An evaluation of CFD for modelling the flow around stationary and rotating isolated wheels, in: SAE Tech. Pap. 980032, 1998.
- [28] S. Diasinos, T.J. Barber, G. Doig, The effects of simplifications on isolated wheel aerodynamics, *J. Wind Eng. Ind. Aerodyn.* 146 (2015) 90–101.
- [29] J. McManus, X. Zhang, A computational study of the flow around an isolated wheel in contact with the ground, *J. Fluids Eng.* 128 (2006) 520.
- [30] A. Morelli, Aerodynamic effects of an automobile wheel, in: MIRA Transl. Number 47/69 A.T.A Vol. 22, 6, 1969, pp. 81–288.
- [31] J.E.J.E. Fackrell, *The Aerodynamics of an Isolated Wheel Rotating in Contact with the Ground*, (Ph.D. thesis), Imperial College of Science and Technology, 1974.
- [32] A. Cogotti, Aerodynamic characteristics of car wheels, in: *Technol. Adv. Veh. Des. Spec. Publ. SP*, 1983, pp. 173–196.
- [33] A.P. Mears, R.G. Dominy, Racing car wheel aerodynamics – comparisons between experimental and CFD derived flow-field data, in: SAE Tech. Pap. Ser., 2004.

- [34] A. Kabanovs, A. Garmory, M. Passmore, A. Gaylard, Investigation into the dynamics of wheel spray released from a rotating tyre of a simplified vehicle model, *J. Wind Eng. Ind. Aerodyn.* 184 (2019) 228–246.
- [35] E. Croner, H. Bézard, C. Sicot, G. Mothay, Aerodynamic characterization of the wake of an isolated rolling wheel, *Int. J. Heat Fluid Flow* 43 (2013) 233–243.
- [36] T. Hobeika, S. Sebben, CFD investigation on wheel rotation modelling, *J. Wind Eng. Ind. Aerodyn.* 174 (2018) 241–251.
- [37] R. Lewis, M. Cross, D. Ludlow, *The Influence of Rotating Wheels on the External Aerodynamic Performance of a Vehicle*, Woodhead Publishing Limited, 2014.
- [38] P. Mannion, Y. Toparlar, B. Blocken, E. Clifford, T. Andrianne, M. Hajdukiewicz, Analysis of crosswind aerodynamics for competitive hand-cycling, *J. Wind Eng. Ind. Aerodyn.* (2018).
- [39] P. Mannion, Y. Toparlar, E. Clifford, M. Hajdukiewicz, T. Andrianne, B. Blocken, The impact of arm-crank position on the drag of a paralympic hand-cyclist, *Comput. Methods Biomed. Eng.* (2019).
- [40] M. Belloli, F. Cheli, I. Bayati, S. Giappino, F. Robustelli, Handbike aerodynamics: wind tunnel versus track tests, *Procedia Eng.* 72 (2014) 750–755.
- [41] B. Blocken, Y. Toparlar, T. Andrianne, Aerodynamic benefit for a cyclist by a following motorcycle, *J. Wind Eng. Ind. Aerodyn.* 155 (2016) 1–10.
- [42] B. Blocken, Y. Toparlar, A following car influences cyclist drag : CFD simulations and wind tunnel measurements, *J. Wind Eng. Ind. Aerodyn.* 145 (2015) 178–186.
- [43] B. Blocken, T. van Druenen, Y. Toparlar, F. Malizia, P. Mannion, T. Andrianne, T. Marchal, G.-J. Maas, J. Diepens, Aerodynamic drag in cycling peloton: New insights by CFD simulation and wind tunnel testing, *J. Wind Eng. Ind. Aerodyn.* 179 (2018) 319–337.
- [44] D. Cleaver, Private communication on September 07, 2018, 2018.
- [45] Campagnolo, Product range catalogue, 1996.
- [46] Campagnolo, Product range catalogue, 1994.
- [47] B. Blocken, Computational Fluid Dynamics for urban physics: Importance, scales, possibilities, limitations and ten tips and tricks towards accurate and reliable simulations, *Build. Environ.* 91 (2015) 219–245.
- [48] J. Franke, A. Hellsten, H. Schlünzen, B. Carissimo, Best practice guideline for the CFD simulation of flows in the urban environment, 2007.
- [49] J. Franke, A. Hellsten, H. Schlünzen, B. Carissimo, The best practise guideline for the CFD simulation of flows in the urban environment : an outcome of COST 732, in: *Fifth Int. Symp. Comput. Wind Eng.*, 2010, pp. 1–10.
- [50] Y. Tominaga, A. Mochida, R. Yoshie, H. Kataoka, T. Nozu, M. Yoshikawa, T. Shirasawa, AJI guidelines for practical applications of CFD to pedestrian wind environment around buildings, *J. Wind Eng. Ind. Aerodyn.* 96 (2008) 1749–1761.
- [51] M. Lanfrat, Best practice guidelines for handling Automotive External Aerodynamics with FLUENT, in: Version 1.2, Fluent Deutschl, GmbH Birkenweg, 14a 64295 Darmstadt/Germany, 2005, pp. 1–14.
- [52] ANSYS inc., *ANSYS Fluent Meshing - User's guide* 18.2, 2017.
- [53] F. Beaumont, R. Taiar, G. Polidori, H. Trenchard, F. Grappe, Aerodynamic study of time-trial helmets in cycling racing using CFD analysis, *J. Biomech.* 67 (2018) 1–8.
- [54] D.M. Fintelman, H. Hemida, M. Sterling, F.X. Li, CFD simulations of the flow around a cyclist subjected to crosswinds, *J. Wind Eng. Ind. Aerodyn.* 144 (2015) 31–41.
- [55] P. Mannion, Y. Toparlar, E. Clifford, M. Hajdukiewicz, T. Andrianne, B. Blocken, On the effects of crosswinds in tandem aerodynamics: An experimental and computational study, *Eur. J. Mech. B* 74 (2019) 68–80.
- [56] T. Defraeye, B. Blocken, E. Koninckx, P. Hespel, J. Carmeliet, Computational fluid dynamics analysis of cyclist aerodynamics: Performance of different turbulence-modelling and boundary-layer modelling approaches, *J. Biomech.* 43 (2010) 2281–2287.
- [57] ANSYS inc., *ANSYS Fluent - Theory guide* 18.2, 2017.
- [58] A.P. Mears, S.C. Crossland, R.G. Dominy, An investigation into the flow-field about an exposed racing wheel, in: *SAE Tech. Pap. Ser.*, 2004.
- [59] B. Blocken, LES over RANS in building simulation for outdoor and indoor applications: A foregone conclusion? *Build. Simul.* 11 (2018) 821–870.
- [60] K. Hanjalic, Will RANS survive LES? A view of perspectives, *J. Fluids Eng.* 127 (2005) 831.
- [61] M. Casey, T. Wintergerste, *ERCOFTAC - special interest group on quality and trust in industrial CFD - Best practice guidelines*, 2000.
- [62] C.R. Kyle, Sunraycer: wheels, tires and brakes, Lecture 3-3, in: *G.M. Sunraycer Case Hist*, Society of Automotive Engineers, Warrendale, Pennsylvania, 1990.